NUCLEAR DATA AND MEASUREMENTS SERIES

ANL/NDM-132

Neutron Interaction
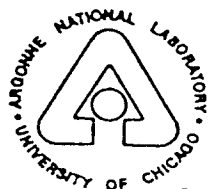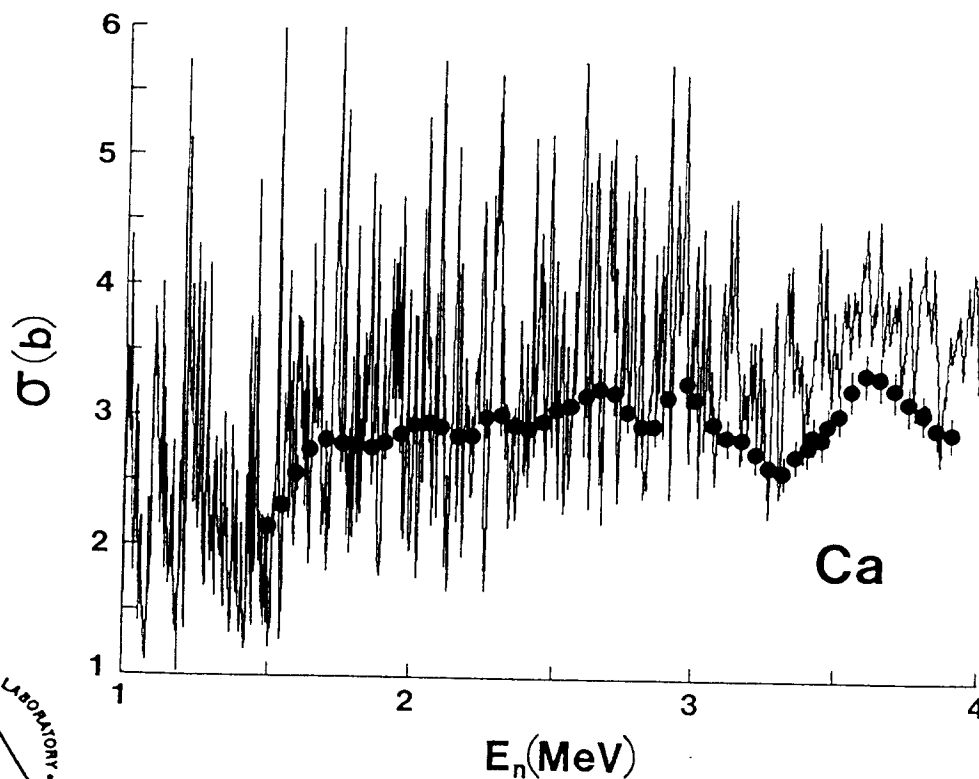## with Doubly-Magic ^{40}Ca

by

A.B. Smith

November 1993

ARGONNE NATIONAL LABORATORY,
ARGONNE, ILLINOIS 60439, U.S.A.

NUCLEAR DATA AND MEASUREMENTS SERIES

ANL/NDM-132

NEUTRON INTERACTION WITH DOUBLY-MAGIC ^{40}Ca

A. B. Smith
November 1993

ARGONNE NATIONAL LABORATORY, ARGONNE, ILLINOIS

Operated by THE UNIVERSITY OF CHICAGO

for the U. S. DEPARTMENT OF ENERGY

under Contract W-31-109-Eng-38

Argonne National Laboratory, with facilities in the states of Illinois and Idaho, is owned by the United States government, and operated by The University of Chicago under the provisions of a contract with the Department of Energy.

NEUTRON INTERACTION WITH DOUBLY-MAGIC ^{40}Ca[*]

by

A. B. Smith

Argonne National Laboratory
Argonne, Illinois
and
The University of Arizona
Tucson, Arizona

Keywords:

Measured $d\sigma/d\Omega_{el}$ and $d\sigma/d\Omega_{inel}$, 1.5 → 10.0 MeV. Optical-statistical, dispersive optical, and coupled-channels models and model systematics. Extrapolation to bound states.

Engineering Physics Division
Argonne National Laboratory
9700 South Cass Avenue
Argonne, Illinois 60439
U. S. A.

NEUTRON INTERACTION WITH DOUBLY-MAGIC ^{40}Ca[*]

by

A. B. Smith

Argonne National Laboratory
Argonne, Illinois
and
The University of Arizona
Tucson, Arizona

PUBLICATIONS IN THE ANL/NDM SERIES

A listing of recent issues in this series is given below. Issues and/or titles prior to ANL/NDM-116 can be obtained from the National Technical Information Service, U. S. Department of Commerce, 5285 Port Royal Road, Springfield, VA 22161, or by contacting the author of this report at the following address:-

Engineering Physics Division
Argonne National Laboratory
9700 South Cass Avenue
Argonne, IL 60439
USA

S. CHIBA, P.T. GUENTHER, R.D. LAWSON, AND A.B. SMITH
Neutron Scattering from Elemental Indium, the Optical Model, and the Bound-State Potential
ANL/NDM-116, June 1990

D.L. SMITH AND L.P. GERALDO
An Evaluation of the Nb-93(n,n')Nb-93m Dosimeter Reaction for ENDF/B-VI
ANL/NDM-117 (November 1990)

J.W. MEADOWS
Characteristics of the Samples in the FNG Fission Deposit Collection
ANL/NDM-118 (November 1990)

S. CHIBA, P.T. GUENTHER, A.B. SMITH, M. SUGIMOTO, AND R.D. LAWSON
Fast-Neutron Interaction with Elemental Zirconium, and the Dispersive Optical Model
ANL/NDM-119, June 1991

A.B. SMITH, P.T. GUENTHER, J.F. WHALEN, AND S. CHIBA
Fast-neutron Total and Scattering Cross Sections of ^{58}Ni and Nuclear Models
ANL/NDM-120, July 1991

S. CHIBA AND D.L. SMITH
A Suggested Procedure for Resolving an Anomaly in Least-squares Data Analysis Known as "Peelle's Pertinent Puzzle" and the General Implications for Nuclear Data Evaluation
ANL/NDM-121, September 1991

D.L. SMITH AND DOMINIQUE FEAUTRIER
Development and Testing of a Deuterium Gas Target Assembly for Neutron Production Via the H-2(D,N)HE-3 Reaction at a Low-energy Accelerator Facility
ANL/NDM-122, March 1992

D.L. SMITH AND E.T. CHENG
A Review of Nuclear Data Needs and Their Status for Fusion Reactor Technology with some Suggestions on a Strategy to Satisfy the Requirements
ANL/NDM-123, September 1991

J.V. MEADOWS
The Thick-Target $^9Be(d,n)$ Neutron Spectra for Deuteron Energies Between 2.6 and 7.0 MeV
ANL/NDM-124, November 1991

A.B. SMITH AND P.T. GUENTHER
Fast-Neutron Scattering Near Shell Closures:- Scandium
ANL/NDM-125, August 1992

A.B. SMITH, J.V. MEADOWS AND R.J. HOWERTON
A Basic Evaluated Neutronic Data File for Elemental Scandium
ANL/NDM-126, November 1992

A.B. SMITH AND P.T. GUENTHER
Fast-Neutron Interaction With Vibrational Cadmium Nuclei
ANL/NDM-127, November 1992

D. L. SMITH
A Least-Sqeares Computational "Tool Kit"
ANL/NDM-128, April 1993

JOSEPH McCABE, A. B. SMITH AND J. V. MEADOWS
Evaluated Nuclear Data Files for the Naturally-Occuring Isotpes of Cadmium
ANL/NDM-129, June 1993

A. B. SMITH AND P. T. GUENTHER
Fast-Neutron Interaction with the Fission Product ^{103}Rh
ANL/NDM-130, September 1993

A. B. SMITH AND P. T. GUENTHER
Fast-Neutron Scattering from Vibrational Palladium Nuclei
ANL/NDM-131, October 1993

TABLE OF CONTENTS

NEUTRON INTERACTION WITH DOUBLY-MAGIC ^{40}Ca

by

A. B. Smith

Argonne National Laboratory, Argonne, Illinois
and
The University of Arizona, Tucson, Arizona

ABSTRACT

Differential neutron elastic- and inelastic-scattering cross sections of elemental calcium (96.94% doubly-magic ^{40}Ca) are measured from $\approx$ 1.5 to 10 MeV with sufficient detail to determine their energy-averaged behavior in the highly fluctuating environment. These results, combined with values previously reported in the literature, are assessed in the contexts of optical-statistical, dispersive optical, and coupled-channels models, applicable to the energy domain 0 → 30+ MeV, with particular emphasis on the lower energies where the interpretations are sensitive to the dispersion relationship and the effective mass. The interpretations define the energy dependencies of the potential parameters (resolving prior ambiguities), suggest that previous estimates of the prominent low-energy (n,p) and (n,α) reactions are too large, reasonably describe observables to at least 30 MeV, and provide a vehicle for extrapolation into the bound-state regime that gives a good description of hole- and particle-state binding energies. The resulting real-potential parameters (in contrast to many ^{40}Ca parameters reported in the literature) are shown consistent with global trends.

I. INTRODUCTORY REMARKS

Elemental calcium very largely consists of the doubly-magic $T = 0$ isotope ^{40}Ca (96.94%). As such, it is essentially the only naturally-occurring doubly-magic element of sufficient mass to be reasonably treated with weak-coupling models. Due to these properties, the neutron interaction with calcium has been extensively studied for more than a quarter of a century [RB67, JM88, MN82, DT88, Hol+69, MS86, MS86A, ARF87, AR87, MS88, Hon+86, Tor+82, OTR90 and Ols+87]. The large majority of the measurements are at incident energies of ≥ 10 MeV despite the fact that much recent physical interest has been in; the lower-energy potential behavior influenced by the dispersion relationship, the effective mass as $E_n \rightarrow 0$, questions as to the interplay between volume and surface absorption, and in a unified potential extending from bound to unbound energies. It is known that the general higher-energy potential parameters are inconsistent with lower-energy data, and it has been suggested [JM88] that there are rather sharp energy dependencies of the geometric potential parameters at lower energies. However, this behavior is not well defined because of the lack of experimental information, understanding that is forbidden to charged-particle probes. It is not surprising that the experimental data base is not well known below ≈ 10 MeV (excepting the total cross section) as the cross sections for the neutron interaction with calcium are known to fluctuate by large amounts. Single or few measurements at isolated energies do not determine the behavior comparable with energy-average model concepts. If the energy-average behavior is to be reliably determined the requisite measurements must be made in great energy detail, and experimental studies in that scope have not been previously attempted in the few-MeV range.

Most of the prior interpretations focused upon higher energies and thus avoided the difficult matter of compound-nucleus (CN) processes. In the case of ^{40}Ca the CN interpretations are considerably complicated by (n,p) and (n,α) channels which have low energy thresholds and remarkably large cross sections at even few-MeV energies [ENDF], collectively approaching a barn. Thus, quantitative calculation of channel competition requires a knowledge of proton and α-particle potentials, and particularly the latter are not well know at these low energies. The experimental knowledge of $^{40}Ca(n,p)$ and (n,α) cross sections is only fragmentary [NNDC]. The interpretive situation is further exasperated by the known collective nature of some of the low-lying levels in ^{40}Ca, notably the 3.7367 MeV (3$^-$) level [Hon+85, Tor+82 and AR87].

In view of the above, from both the experimental point of view and that of the model interpretations, the fast neutron interactions with ^{40}Ca are an enigma fraught with uncertainties in the low-energy

1

(< 10 MeV) region where the physical representations are presumed to be rather rapidly changing. Thus it is not surprising that the various attempts to extend the physical interpretations into the lower-energy regime are not particularly consistent within themselves, nor with global trends. For example, many of the interpretations employ real-potential reduced radii of ≈ 1.2 fm, in contrast to what one would expect from the general trend of increasing real radii with decreasing target mass [SG92, Mey73], and ^{40}Ca is a relatively light target.

The present work was undertaken some time ago in an effort to resolve some of the above issues. It proved a difficult experimental and interpretive endeavor that extended over a number of years, and which lead to an ancillary study of similar neutron interactions with the nearby nucleus ^{45}Sc [SG93]. Section II outlines the experimental methods. Section III presents the results of the detailed measurements. Section IV deals with the optical-statistical, dispersive-optical and coupled-channels models and their application. Section V discusses the results, including extrapolation of neutron model to the bound-energy regime and the relation of the present work to systematic physical and model trends.

The above remarks focus on fundamental physical concepts. However, it should be noted that calcium (i.e., ^{40}Ca) is a major constituent of concrete, a material that is widely used in nuclear-engineering applications for shielding, and that calcium is a significant component of many biological systems. As such, accurate knowledge of the basic nuclear data governing the fast-neutron interaction with calcium is of considerable applied concern and has the potential for large social benefits. The present work provides such applied information, and implies other applications-important fundamental data (e.g., ^{40}Ca (n,p) and (n,α) cross sections).

II. OUTLINE OF EXPERIMENTAL METHODS

The neutron-scattering measurements of the present work were carried out using the fast-neutron time-of-flight technique [CL55]. This method has long been employed at Argonne National Laboratory in neutron-scattering studies using a ten-angle detection system, and has been extensively described elsewhere [Smi+67, Bud+84 and Chi+92]. Thus only a very brief outline will be given here, with emphasis on those facets of the method that are particularly relevant to the present work, or which represent some change from the procedures previously reported.

The measurement sample consisted of a cylinder of metallic elemental calcium (chemical purity 99+%), 2 cm in diameter and 2 cm long. It was sealed in a stainless-steel can 0.125 mm thick to avoid oxidation, and an equivalent-sized empty container was used for background determinations. This is a relatively small sample that provided "good" scattering geometry. However, the nuclear density of elemental calcium is low, and thus detector response rates with the small sample were modest. This limitation was partly compensated for by the high transmission of the sample, and thus small multiple-event corrections. Similarly sized samples of polyethylene (CH_2) and pile-grade graphite were used in the detector-normalization procedures.

The scattering samples were placed $\approx$ 18 cm from the neutron source at a 0° source-reaction angle, and at the focus of ten flight paths. The concurrent use of ten flight paths provided the measurement efficiency and stability making practical the very extensive measurements required for energy-average scattering cross section determinations in the highly fluctuating environment of calcium scattering at energies of less than $\approx$ 10 MeV. The flight paths were tightly collimated and $\approx$ 500 cm long. One or two additional time-of-flight detectors were used to monitor the source intensity. The scattered-neutron detectors were liquid organic scintillators of $\approx$ 2 cm thickness and $\approx$ 12.5 cm diameter. The overall effective scattered-neutron resolution was $\approx$ 0.6 ns/m.

Below energies of 4.0 MeV, the $^7Li(p,n)^7Be$ neutron-source reaction was used [Dro87]. The lithium targets consisted of evaporated metal films of a thickness necessary to provide the desired neutron energy-spread at the sample. Above 4.0 MeV, the D(d,n)T neutron-source reaction was employed [Dro87]. The target deuterium gas was contained in a cell $\approx$ 2.5 cm long, with the gas pressure adjusted to provide the desired neutron energy spread at the scattering sample. These sources were pulsed at a repetition rate of 2 MHz, with burst durations of $\approx$ 1 ns. Burst intensity was enhanced by the use of a harmonic ion-bunching system.

The relative energy responses of the ten scattering detectors were determined by the observation of the neutrons emitted from the spontaneous fission of ^{252}Cf [SGS77]. At energies below 4.0 MeV the measurements were normalized to the well-known neutron total cross section of elemental carbon [CSL82] as described in ref. [SGM82]. Above 4.0 MeV the measurements were made relative to the standard H(n,n) cross section [CSL82]. Data acquisition, reduction to cross sections, and corrections for multiple-event, attenuation and angular-resolution effects were handled by an integrated computer software system providing accurate and efficient data

3

flow [Gue77, Smi88].

Inelastic neutron-scattering cross sections were determined concurrently with the measurement of the elastic-scattering angular distributions using the ≈ 5 m flight paths, as outlined above. At incident energies above ≈ 7 MeV, additional attention was given to scattered neutrons due to the excitation of the first few levels in calcium. A heavily-shielded source and a 15.6 m flight path at a scattering angle of 80° was employed to optimize the scattered-neutron resolution. This system was identical to that described in ref. [Chi+92], and provided scattered-neutron resolutions of better than 0.3 ns/m.

III. EXPERIMENTAL RESULTS

The goal of the present experimental measurements was the provision of a comprehensive data base that defines the energy-averaged behavior of the neutron scattering from calcium at energies of ≤ 10 MeV. The elastic-scattering process was a primary consideration, with secondary attention to the inelastic excitation of the first few levels in ^{40}Ca. The neutron total cross section is sufficiently known for the present considerations [ENDF, LHH80], and thus redundant measurements were not undertaken.

III-1. Elastic Scattering

The main experimental problem was the determination of a reliable energy-averaged behavior in the context of a very fluctuating cross section. That problem is most acute below ≈ 4 MeV where there must be a compromise between the resolution of the elastic and inelastic contributions and the reasonable determination of the energy-average trends. These conflicting requirements were effectively addressed using the Argonne multi-detector system.

Below ≈ 4 MeV the elastic angular distributions are not rapidly changing with angle thus suitable angular definition was obtained with ten differential measurements at each energy, distributed between ≈ 20° and 160°. The uncertainties in these differential values were approximately 5%, including statistical, systematic and angle-normalization contributions. The measurements were made from incident energies of < 1.5 MeV to 4.0 MeV, with incident-energy spreads of ≈ 50 keV, and in 50 keV incident-energy steps. This procedure assured a complete coverage of the experimental energy range, including response from all the resonance structure. The measurement regime resulted in approximately 500 differential cross

4

sections, and was practical only with the above-cited multi-detector system. The use of the system is not only a matter of efficiency, but it also assures that an entire distribution is obtained concurrently, thus avoiding possibly-large distortions that can result from small variations in incident-energy spread, or in the absolute-energy scale, from angular measurement to measurement. Such perturbations are inevitable to some extent, and can have a violent effect when using a single (or few) detector (s) to map out an angular distribution in the context of a very rapidly fluctuating cross section.

The angular distributions obtained in the above low-energy measurements were very energy dependent, reflecting the underlying resonance structure. This is explicitly illustrated in reference [SG82], which is a preliminary report of the lower-energy portion of the present work. These fluctuations were partially smoothed by averaging the measured data over a 250 keV energy interval, with the results shown in Fig. III-1. There are some energy-dependent variations in the distributions of Fig. III-1, but the energy-average trends are reasonably mapped out. The measured differential distributions were least-square fitted with Legendre-polynomial expansions to obtain the corresponding angle-integrated elastic-scattering cross sections. These are compared with the fluctuating total cross section in Fig. III-2. The average energy-dependent trends of the high-resolution total cross sections are very well represented by the angle integrated elastic-scattering cross sections up to ≈ 3 MeV. Above that energy the elastic scattering increasingly falls below the general trend of the total cross sections due to the opening of inelastic channels and to the rapidly increasing magnitudes of the (n,p) and (n,α) cross sections [ENDF].

While the fluctuations of the elastic-scattering cross sections persist to 8 - 10 MeV, they are not as violent as at lower energies. Therefore an experimental approach differing from that above was adopted for measurements from 4.5 to 10 MeV. In this range the measurements were made at intervals of ≈ 0.5 MeV. Thirty or more differential values were obtained at each energy, distributed between $\approx 20^{0}$ and 160^{0}. Incident-energy spreads were intentionally kept relatively large (e.g., 200 keV or more) in an effort to smooth fluctuations. However, such broad incident-energy spreads compromised the ability to resolve discrete inelastically-scattered neutron groups. This approach appeared to be successful in averaging the elastic-scattering fluctuations above ≈ 6 MeV, but there was some indication that fluctuations were still a problem at 4 - 5 MeV as measurements taken at different times occasionally systematically differed from one another, probably as the result of small differences in incident-energy scale or incident-energy spread. The experimental uncertainties ranged from a few to ten percent or more at the minima of the distributions. These minima are very deep at some energies (only several mb/sr). The present higher-energy elastic-scattering

5
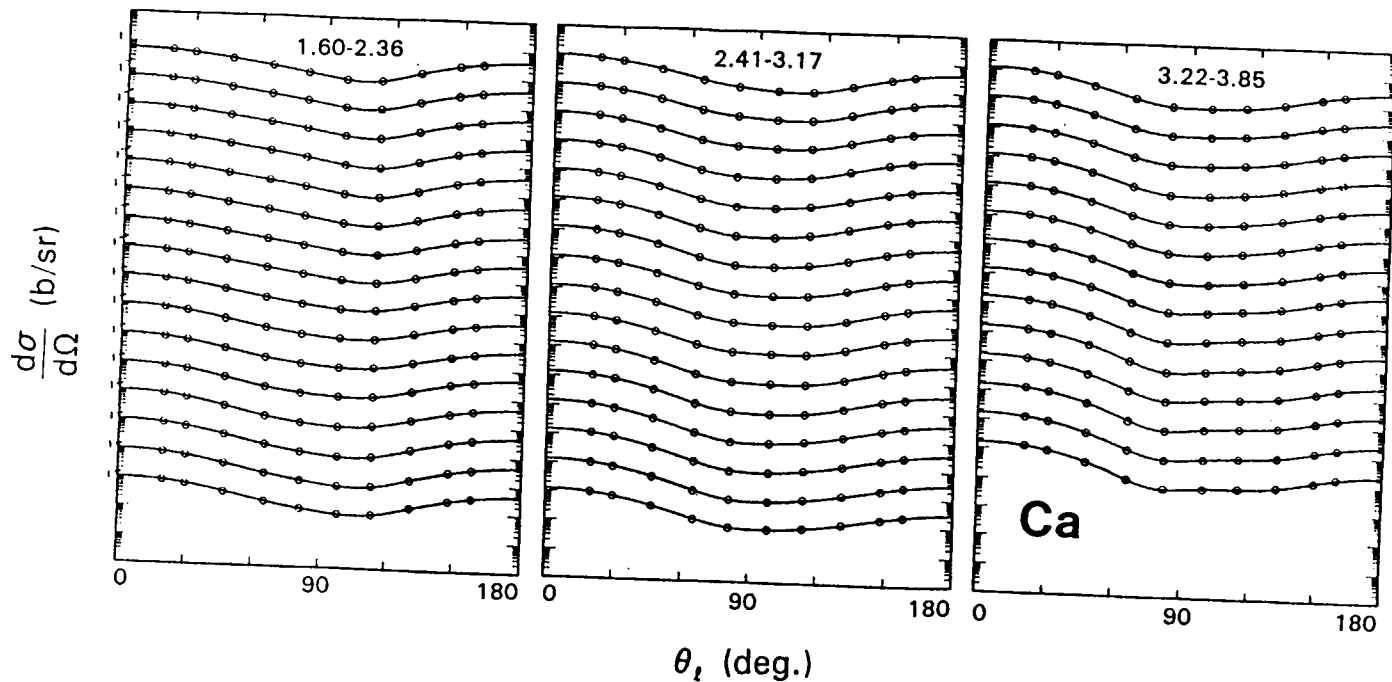
Fig. III-1. 250 keV averages of the present calcium elastic-scattering results over the energy range ≈ 1.5 to 4.0 MeV. The experimental values are indicated by symbols, and curves denote the results of fitting Legendre-polynomial expansions to the measured values. The energies of the distributions are approximately equally distributed over the energy ranges numerically indicated in each section of the figure. (Throughout this paper cross sections are given in the laboratory coordinate system).

Fig. III-2. Comparison of high resolution total cross sections of calcium (curve) [ENDF, LHH80] with the broad-resolution elastic-scattering results of the present work (symbols).

results are illustrated in the 4.5 to 10.0 MeV portion of Fig. IV-1.

There are a number of previously-measured calcium elastic-scattering results reported in the literature, most of them at energies above those of the present work. Furthermore, detailed comparisons are difficult as the energy-isolated values found in the literature may have slightly different incident energies or energy spreads than those of the present work. In the context of the highly fluctuating calcium cross section, these small energy differences can lead to very discrepant results. Despite these concerns, comparisons of the elastic-scattering results of the present work with those reported in the literature are reasonably encouraging. Some examples are given in Fig. III-3.

III-2. Inelastic Scattering

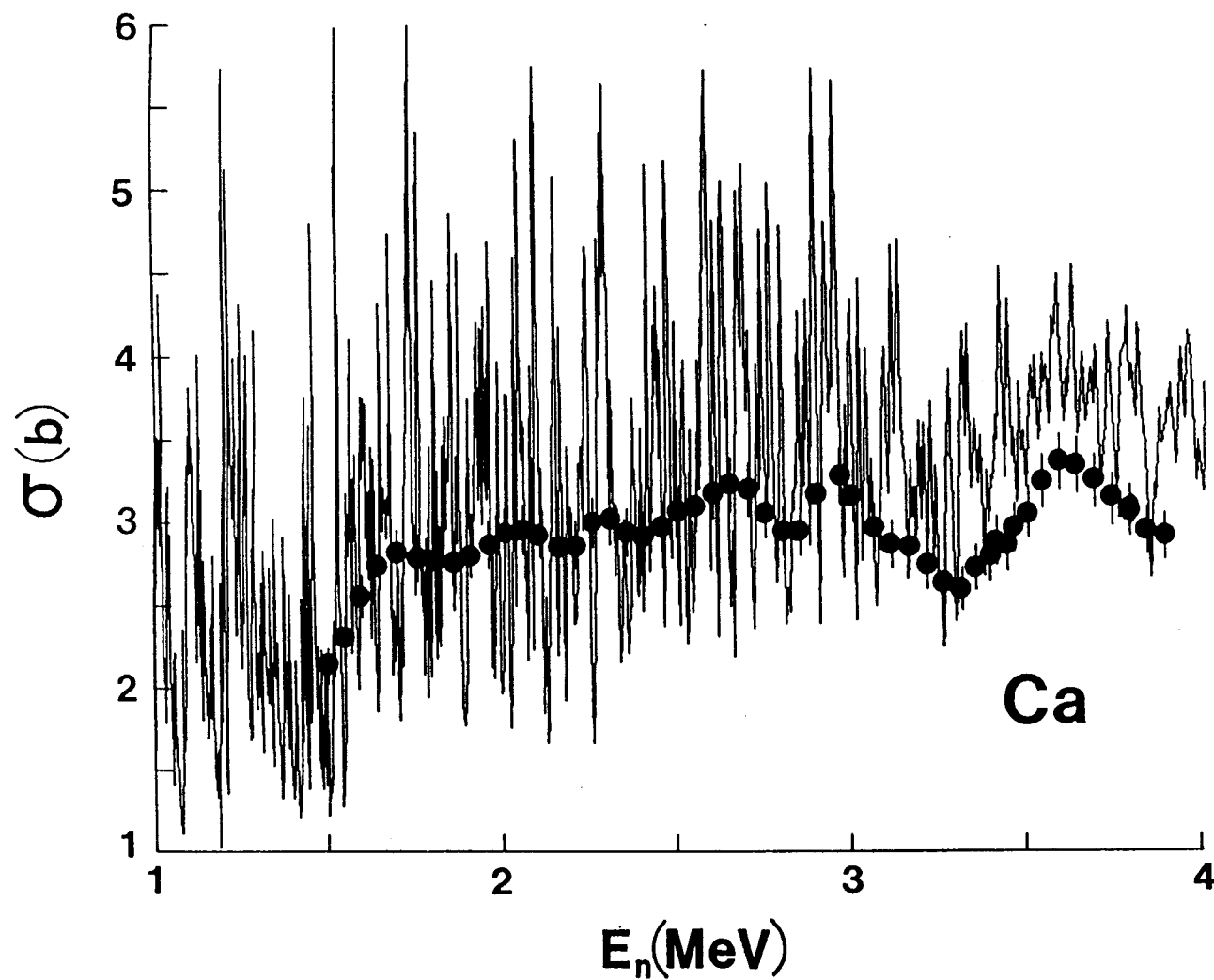The inelastic-scattering cross sections are a key to the definition of the compound-nucleus cross sections, and these are a matter of considerable importance in the interpretations, as described in Section IV. Moreover, the experimental knowledge of inelastic-neutron scattering from calcium is remarkable sparse, largely confined to the work of Perey and Kinney [PK70]. Thus, the present inelastic-scattering measurements contribute substantive information of both basic and applied interest.

The excited level structure of ^{40}Ca is well known up to at least 8 MeV [EL78]. The first excited level is at 3.3526 MeV (0^+), and the corresponding differential inelastic-scattering cross sections were determined to ≈ 8.4 MeV in the present work (throughout these remarks, the angle-integrated inelastic-scattering cross sections were determined by fitting the observed differential values with a Legendre-polynomial series). The experimental results were determined concurrently with the elastic-scattering distributions, described above, and from measurements using smaller incident-energy spreads (e.g., ≈ 100 keV) and the long, high-resolution, flight path outlined in Section II. The experimental velocity resolution obtained with the high-resolution measurements is illustrated in Fig. III-4. The present experimental values are very consistent with those of refs. [PK70, BQ81 and Bai+77], and quite small. The next excited level is at 3.7367 MeV (3^-). The present work, and that of ref. [PK70], give fragmentary knowledge of the corresponding inelastic-scattering cross section as it is difficult to resolve this contribution from that due to the next level at 3.9044 MeV (2^+). However, the experimental information does indicated that the cross section is relatively large (e.g., ≈ 200 mb at 5.5 MeV). Far more comprehensive experimental knowledge of the composite cross section for the excitation of the 3.7367 and 3.9044 MeV levels was obtained in the present work and that

8
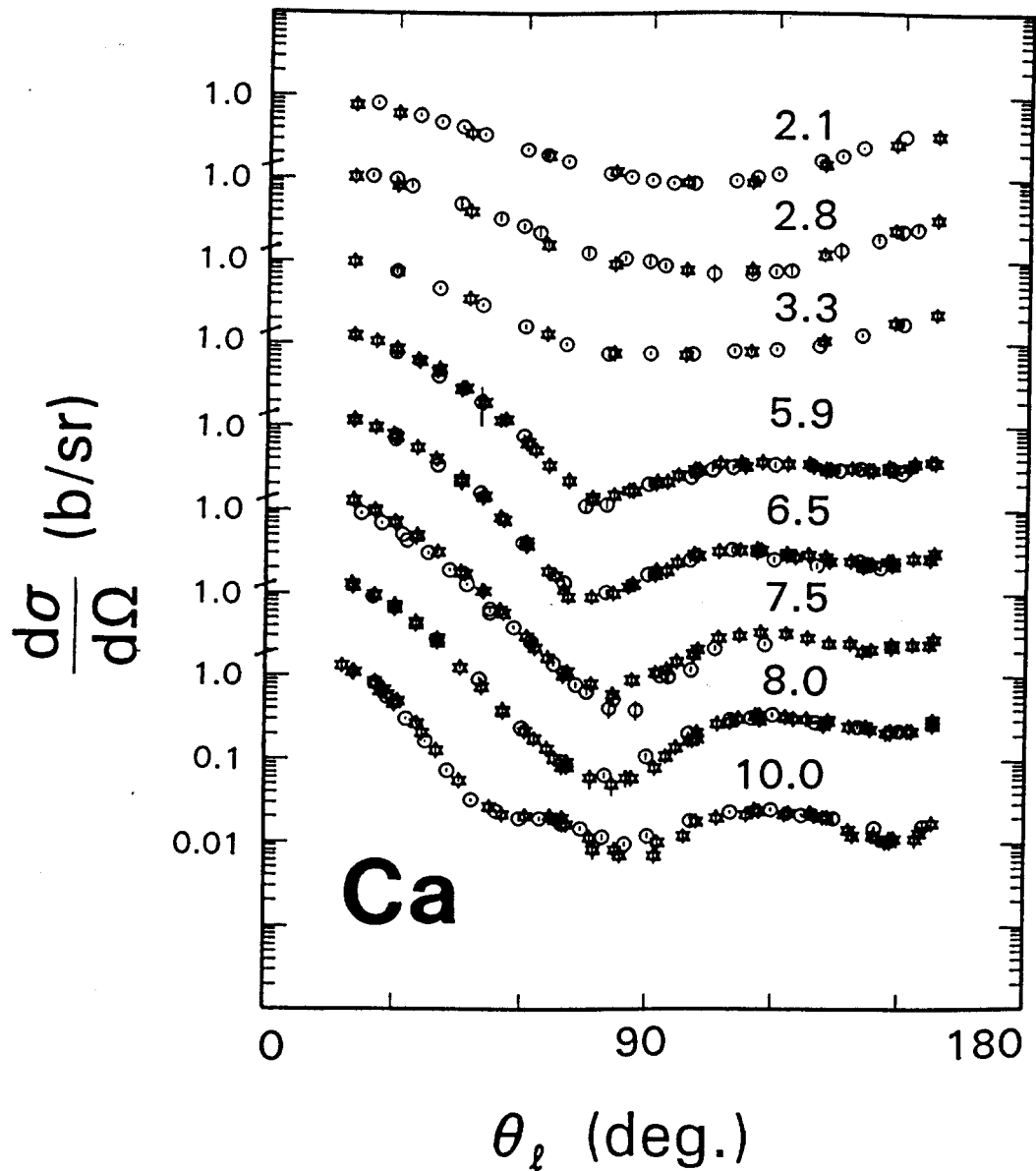
Fig. III-3. Some illustrative comparisons of the present elastic-scattering results ("star" symbols) with those reported in the literature (circular symbols) [PK70, RB67, Tor+82, Hol+69 and Abr+71]. Approximate incident energies are numerical noted in MeV.
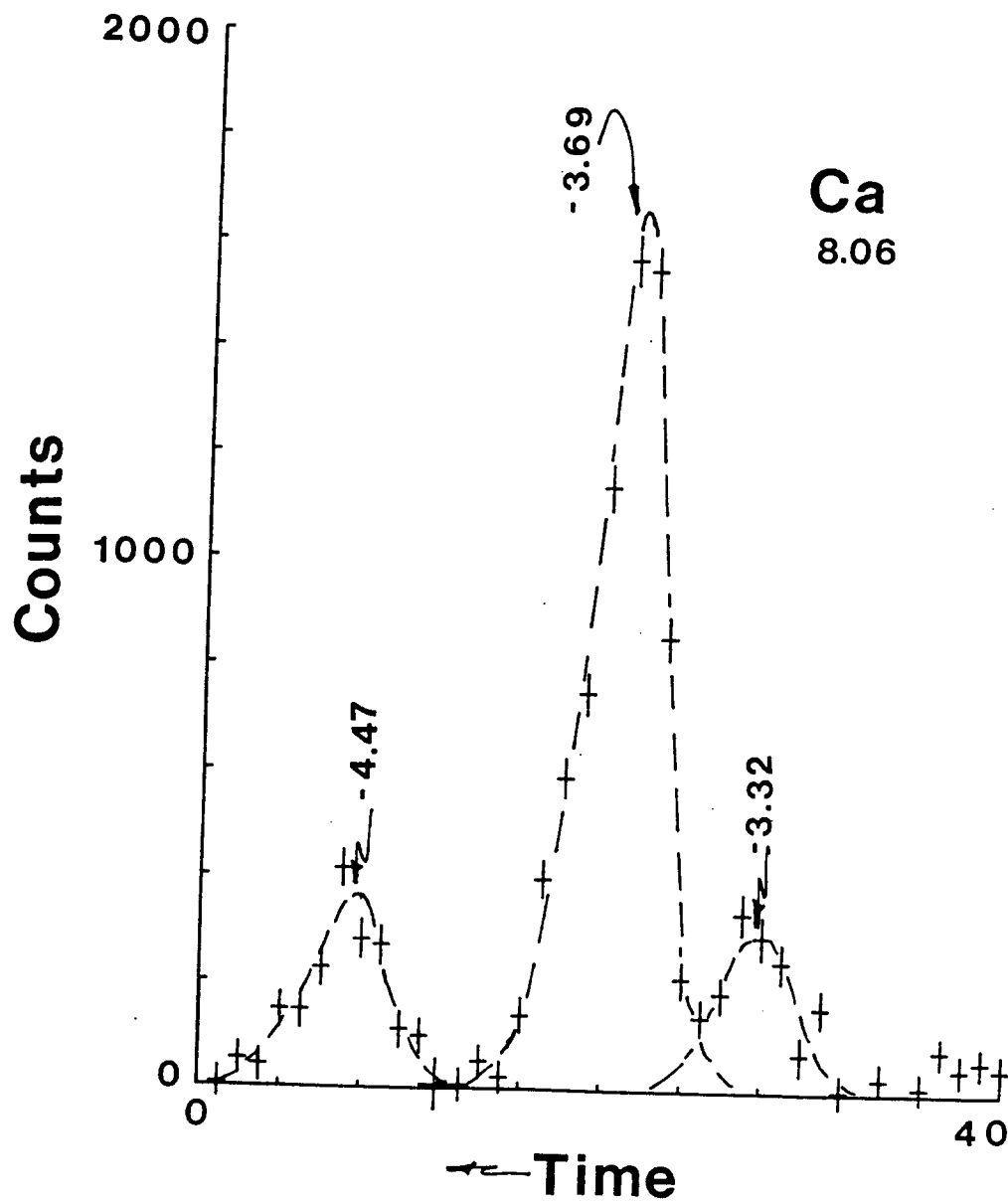
Fig. III-4. Illustrative time spectrum obtained with the ≈ 15 m flight path at an incident neutron energy of 8.06 MeV and a scattering angle of 80°. The time is in units of nsec. The Q-values implied by this particular measurement are numerically indicated in MeV.

10

of ref. [PK70]. The experiments indicate that, qualitatively, the cross sections for the excitation of each of these two states are approximately the same at lower energies. The composite cross section is relatively large (e.g., at ≈ 5 MeV it is several hundred mb). What is commonly measured and reported in the literature is the cross section for the combined excitation of the 3.3526, 3.7367 and 3.9044 levels, and the experimental results indicate a large composite cross section at lower energies (peaking at ≈ 400 mb), and which continues with modest values to higher incident energies [PK70, Bai+77, Tor+82, Hon+86, AR87, Hic+90 and OTR90]. The next excited level is at 4.4914 MeV (5$^-$). Results from the present work and that of ref. [PK70] are in good agreement, and the cross sections are small. The next two levels are at 5.2116 (2$^+$) and 5.2488 (4$^+$), and the individual cross sections were not experimentally resolved. However, the combined cross section is small in both the present work and that of ref. [PK70]. The next two levels are at 5.6135 (4$^-$) and 5.6295 (2$^+$), and, again, the corresponding scattered-neutron groups were not experimentally resolved. The respective combined cross sections of the present work and that of ref. [PK70] are not large. Above ≈ 6.0 MeV, the excited level density increases very rapidly and there is little definition of discrete inelastic-scattering cross sections in the present, or any other, work. There is limited information about the cross sections for the excitation of the triplet of levels at 5.903, 6.026 and 6.030, but the corresponding cross sections are only qualitative as determined from this work, or that of ref. [PK70]. The above angle-integrated cross sections of the present work are summarized and compared with the corresponding values given in the literature in Fig. III-5.

The angular distributions of neutrons scattered in the above inelastic processes were determined in the present measurements. The characteristic feature at lower energies was an approximate symmetry about 90°. This is the type of distribution to be expected from processes that are primarily of a CN nature. Even at 10 MeV, there is only modest indication of the forward peaking of the distributions that is characteristic of direct reactions. At much higher energies (e.g., ≈ 15 - 20 MeV) the literature indicates that this is no longer true, but the corresponding cross sections are small [Bai+77, Hon+86, AR87, Hic+90 and OTR90]. These anisotropies and direct-reaction processes are discussed in Section IV.
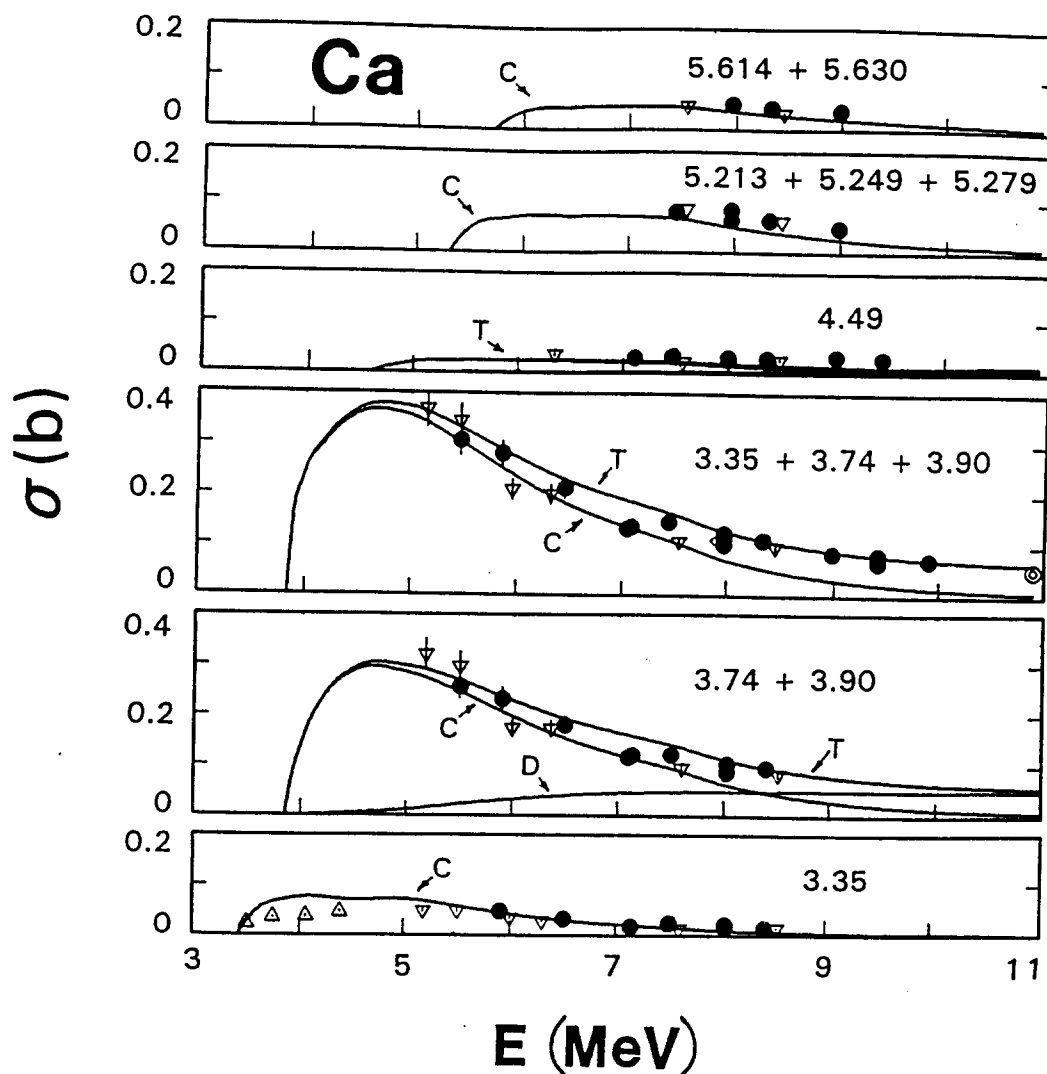
Fig. III-5. Measured inelastic-neutron-excitation cross sections of elemental calcium. The experimental results of the present work are indicated by solid symbols, and those of ref. [PK70] by ∇. Additional measured values [Hic+90, Bai77 and BQ81] are noted by various other symbols. Curves indicate the results of calculations as described in the text, where "C" denotes CN contributions, "D" those of direct reactions, and "T" the sum of the two. The contributing excitation energies (in MeV) are given numerically in each section of the figure.

IV. PHYSICAL MODELS

IV-1. Experimental Data Base

All of the present model interpretations employed the same data base. The primary foundation consisted of the differential elastic-scattering cross sections and was constructed as follows:-

i) Below 1.5 MeV the scattering data of ref. [Lan+66] were used. These are total-scattering results, but they are all well below the inelastic-scattering thresholds thus are equivalent to elastic scattering. This set of data was obtained with relatively broad experimental resolutions and is in considerable energy detail. Thus, despite the highly resonance nature of the cross sections at these energies, broad energy averages of these results should be reasonably consistent with the concepts of energy-averaged models. Averaging increments of 400 keV were selected as a compromise between energy dependence and energy average.

ii) From 1.5 to 4.0 MeV the detailed experimental results of the present work were used. These results were averaged over additional increments of $\approx$ 300 keV. This averaging increment was a compromise between the determination of the energy-averaged behavior and, at the same time, the provision of reasonable definition as various inelastic-scattering and (n,X) channels open. These two objectives are conflicting, thus the results near the prominent inelastic thresholds at about $\approx$ 3.7 MeV should be considered with some circumspection.

iii) From 4.0 to 10.0 MeV, the results of the present work were used. As described above, these results were obtained with rather broad incident-neutron resolutions that, hopefully, averaged the underlying structure. This assumption may not be as appropriate at the lower-energy limit of the energy interval. The literature contains some additional data relevant to this energy range [PK70, RB67 and Hon+86]. It was not used in the model derivations due to its limited scope.

iv) From 10.0 to 30.4 MeV, the data base was constructed from the information reported in the literature, as available at the National Nuclear Data Center [Fra+64, Bai77, FCR77, Rap+77, Dev+81, Tor+82, Hon+86, ARF87 and Ols+87]. Some addition data from the Center were abandoned as being grossly discrepant with the body of information and/or as being of relatively limited scope. Even within the accepted data there were clearly differences. These generally appeared to be random, but in some cases there is evidence of systematic discrepancies associated with the particular institutions involved. It was hoped that the sample, consisting of 13 distributions, was large enough to average these differences. There is a higher-energy distribution (40 MeV) reported in the literature [Dev+81], but it lacks definition at scattering angles back of $\approx 90^{\circ}$ so it was not used

in the data base.

The experimental uncertainties to be associated with the present elastic-scattering data are reasonably defined. Those relevant to other aspects of the data base are less certain, or non-existent in some cases. Where uncertainties were cited by the various authors (often only statistical estimates) they were used in the fitting procedures. Where no error was given by the author(s), it was assumed that the relative differential cross-section uncertainty was inversely proportional to cross section magnitude.

A key factor in the model interpretations was the neutron inelastic-scattering cross sections due to the excitation of the first three levels. These are reasonably defined, as discussed in Section III, and primarily result from the present work and that of ref. [PK70]. Associated considerations in the model interpretations are the (n,p) and (n,α) cross sections at lower energies (e.g, below $\approx$ 12 MeV) where compound-elastic scattering is a significant concern. Due to the nature of the processes, the experimental knowledge of ^{40}Ca (n,p) and (n,α) total reaction cross sections is only fragmentary [NNDC]. For the present interpretations the energy-dependencies (not the magnitudes) of the (n,p) and (n,α) cross sections of ^{40}Ca were taken from the ENDF/B-VI file [ENDF].

In addition to the above differential data, the model determinations also considered the neutron total cross sections to $\approx$ 40 MeV. These were taken from the measured values of Larson et al. [LHH80], extended to lower energies using the resonance behavior given in ENDF/B-VI. The total cross section is highly fluctuating to at least 5 MeV, and thus broad energy averages are necessary for energy-average model comparisons. Neutron polarizations were given minor consideration in the interpretations, using the experimental results of refs. [Hon+86 and Tor+82].

IV-2. Potential Form Factors

Throughout the model interpretations it was assumed that the real potential had a Saxon-Woods (SW) form factor, the imaginary potential a SW-derivative form, and that the spin-orbit potential was real with a Thomas form [Hod71]. An imaginary spin-orbit potential has been reported [Hon+86] but it is small, and later work attributes the contribution to an artifact as a consequence of inattention to dispersion effects [DT88]. Thus, an imaginary spin-orbit potential was ignored. It was further assumed that the elemental data used in the interpretation consisted entirely of ^{40}Ca ($\approx$ 97% abundance). With this assumption T = 0 and all aspects of the potential are isoscaler. Potential strengths will generally be presented here in the form of

14

volume-integrals-per-nucleon, J_i, where

$$J_i = \frac{4\pi}{A} \int_0^\infty U_i(r) \, r^2 \, dr, \qquad (IV-1)$$

and radii, R_i, will be defined by r_i, where $R_i = r_i \cdot A^{1/3}$.

IV-3. Spherical Optical Model (SOM)

The interpretation of neutron scattering from calcium above incident energies of $\approx 10 \rightarrow 12$ MeV is relatively simple as a great number of CN channels are open. As a consequence, the individual CN processes (particularly the compound-elastic (CE) process) are very small and the elastic-scattering can be treated as shape-elastic (SE) scattering. At lower energies, which are primarily addressed in this work, the CN processes are important and can not be ignored, including the (n,p) and (n,α) channels. Thus, in a full scope, the model interpretations should treat charged-particle and neutron-emission CN exit channels. Model derivation by explicit fitting of experimental data in such a comprehensive scope has not been attempted as the calculations are very large, the requisite experimental charged-particle data is not available to sufficient accuracy, and charged-particle potentials are not well defined.

An alternative to the above complexities and uncertainties is the use of a "global" model to determine CE contributions, "correcting" the observed elastic-neutron-scattering data for the CE component, and then treating the "corrected" result with simple SE fitting. Essentially that approach was used in ref. [JM88]. However, it introduces the global model into the interpretations and as a result may lead to distortions, particularly as the necessary charged-particle potentials remain uncertain at lower energies.

Another alternative is an iterative approach based upon the neutron observables. Using the higher-energy neutron data in a region where the CE contributions can be reasonably ignored, a first estimate of the potential is obtained by the explicit fitting of the elastic-scattering neutron data assuming the equivalence of experimental and SE scattering. This estimate is then used to calculate the lower-energy CN processes, ignoring charged-particle competition. The resulting calculated inelastic-scattering cross sections of the first three levels are then compared with the reasonably known experimental values to obtain a CN adjustment factor which is assumed applicable to all CN neutron channels, including the CE channel. The adjusted CE contribution to the observed elastic scattering is subtracted to obtain "elastic" cross sections that are suitable for simple SE fitting. The fitting process is then carried

out over the full energy range, a new model obtained, and corrections re-determined in an iterative manner. This method, dependent only on the observed neutron cross sections, was used throughout the present work. Since the prominent ^{40}Ca inelastic-scattering cross sections are best known from $\approx$ 5 → 6 MeV with little direct-reaction contribution, that energy range was used for obtaining the above CN adjustment factor. The factor was extrapolated to other energies using only the energy-dependent shape of the (n,p) and (n,α) cross sections as given in ENDF/B-VI [ENDF] and the calculated absorption cross sections. The shapes of the (n,p) and (n,α) cross sections at lower energies are strongly influenced by coulomb-barrier effects and thus should be reasonably reliable. The normalization of the composite magnitude of the (n,p) and (n,α) cross sections follows directly from the absorption and inelastic-scattering cross sections calculated with the model, and the observed inelastic-scattering cross sections. Thus, the procedure implies a total (n,X) cross section from the observed neutron processes that can be compared with otherwise-determined results.

The above iterative approach requires detailed CN calculations. The excited level structure of ^{40}Ca is relatively sparse due to its doubly-magic nature, and thus CN calculations (and CE "adjustments" to the observed elastic scattering) are a concern to relatively high energies, in the present work to 12 MeV. Twenty five discrete excited levels were considered in the calculations, to excitations of $\approx$ 7.3 MeV, with level energies and J^π values taken from ref. [EL78]. Higher-energy excitations were represented using the statistical formalism of Gilbert and Cameron [GC65]. All the spherical-model calculations were carried out using the spherical optical-statistical code ABAREX [Mol82]. That code treats statistical processes using the Hauser-Feshbach formula [HF52], including resonance width-fluctuation and correlation corrections as given by Moldauer [Mol80]. The latter corrections give results similar to those obtained with the method of Hofmann et al. [Hof+75].

At each iteration, after the observed differential elastic scattering cross sections were "adjusted" for CE contributions they were chi-square fitted to determine the optical potential. First the real-potential geometry was determined (its behavior should be relatively "global"), then the imaginary-potential geometry was determined (it may depend upon the specific details of the nuclear structure), and finally the real and imaginary potential strengths were determined. The steps at each iteration were as follows:-

i) Six parameter fitting varying real and imaginary strengths, radii and diffusenesses was carried out. From this the real diffuseness, a_v, was fixed. Experience has shown this parameter to be relatively uncorrelated with the five others, energy independent and of a "global" nature [Chi+90].

16

ii) With a_v fixed, five parameter fitting was used to determine the real-potential radius, r_v. The real-potential magnitude is strongly anti-correlated with r_v, increasing the scatter in the r_v determined from the fitting [Smi93].

iii) The imaginary radius, r_w, was next addressed using four parameter fitting with the real geometry fixed to the above values. r_w is not strongly correlated with the other imaginary parameters.

iv) The imaginary diffuseness, a_w, was then determined with three-parameter fitting and the above geometric parameters. It is strongly anti-correlated with the imaginary strength, and thus the results tend to scatter [Smi93].

v) Finally, two-parameter fits, with the geometries fixed to the above values, were carried out to determine the real and imaginary potential strengths.

The above five-step procedure has been successfully employed in a number of cases (e.g., refs. [Chi+90, Chi+92 and Smi+92]) and gives good results. All of the present fitting a-priori assumed the real spin-orbit potential of Honore et al. [Hon+86]. This spin-orbit potential was developed from extensive polarization studies. The present fitting of elastic-scattering is not particularly sensitive to the details of the spin-orbit potential.

After three iterations of the above CE-adjustment and SE-fitting procedures, the SOM parameters reasonably converged to the values given in Table IV-1. These parameters are similar to those encountered in previous work at this laboratory [Chi+90]. The physical aspects will be discussed in some detail in Section V. However, at this point it should be noted that:-

i) There was no experimental support for a volume absorption in the present interpretations.

ii) $r_w > r_v$ at lower energies, and decreases with energy. Such a behavior was noted long ago [Mol63].

iii) r_v is constant at higher energies with a value larger than that of some reported ^{40}Ca interpretations, but is smaller at very low energies.

iv) J_v decreases and J_w increases with energy, as one would qualitatively expect from the Hartree-Fock behavior and the opening of channels with increasing energy, respectively,

v) While the a_v is reasonably constant, a_w becomes quite small as $E \rightarrow 0$.

Clearly, the geometric parameters of the model are energy dependent as qualitatively suggested by Johnson and Mahaux [JM88] for ^{40}Ca, and more generally by work at this laboratory. It should also be pointed out that the above iterative interpretation implies an $(n,X) \equiv (n,p) + (n,\alpha)$ cross section that is $\approx$ 10 - 15% smaller than that given in ENDF/B-VI.

The SOM potential of Table IV-1 provides an acceptable description of the data base from which it was primarily developed, as illustrated in Fig. IV-1. Notable is the good agreement at lower energies where CE contributions are large. Between $\approx$ 10 and 14 MeV there are some shortcomings in the descriptions at angles of $\approx 120^0 \rightarrow 140^0$. This is probably a manifestation of a fundamental aspect of the process that is not entirely consistent with the energy-averaged models as the same discrepancies are evident in several similar interpretations found in the literature [Tor+82, DT88 and JM88]. The parameters of Table IV-1 also provide an acceptable description of the observed total cross section to more than 40 MeV, as illustrated in Fig. IV-2. There is some uncertainty near 3 - 4 MeV, as, even in the 500 keV averages of the experimental data used in the figure, there is a considerable amount of residual structure. It is notable that the calculations reasonably predict the total cross sections at low energies in contrast, for example, to the results obtained with the general potential of ref. [JM88]. The potential of Table IV-1 also provides a good description of the CN inelastic-scattering cross sections at lower energies, as illustrated in Fig. III-5. However, this agreement is somewhat compromised as the observed inelastic-scattering cross sections have been used to guide the potential derivation, as outlined above. Finally, the potential of Table IV-1 leads to acceptable descriptions of the observed scattered-neutron polarizations, as illustrated in Fig. IV-3. Extensive SOM studies, largely focusing on the polarizations, have obtained only marginally better results [Tor+82].

IV-4. Dispersive Optical Model (DOM)

There is a well-known dispersion relationship between the real, V, and imaginary, W, portions of the SOM [Sat83]

Table IV-1. SOM parameters resulting from the chi-square fitting procedures (energies E are given in MeV, strengths J_i are in volume integrals per nucleon with the dimension of MeV-fm^3, strengths V_i are in MeV, and geometric terms are in fms.).

Real Potential

$$J_v = 504.0 - 2.710 \cdot E$$
$$r_v = 1.15 + 0.0159 \cdot E \quad (E < 8)$$
$$r_v = 1.2770 \quad (E \geq 8)$$
$$a_v = 0.5965$$

Imaginary Potential

$$J_w = 55.0 + 2.75 \cdot E \quad (E < 20)$$
$$J_w = 110.0 \quad (E > 20)$$
$$r_w = 1.350 - 0.0068 \cdot E \quad (E < 11)$$
$$r_w = 1.275 \quad (E \geq 11)$$
$$a_w = 0.260 + 0.0252 \cdot E \quad (E < 10)$$
$$a_w = 0.5121 \quad (E \geq 10)$$

Spin-Orbit Potential [Hon+86]

$$V_{so} = 5.42 - 0.0240 \cdot E$$
$$r_{so} = 1.020$$
$$a_{so} = 0.500$$
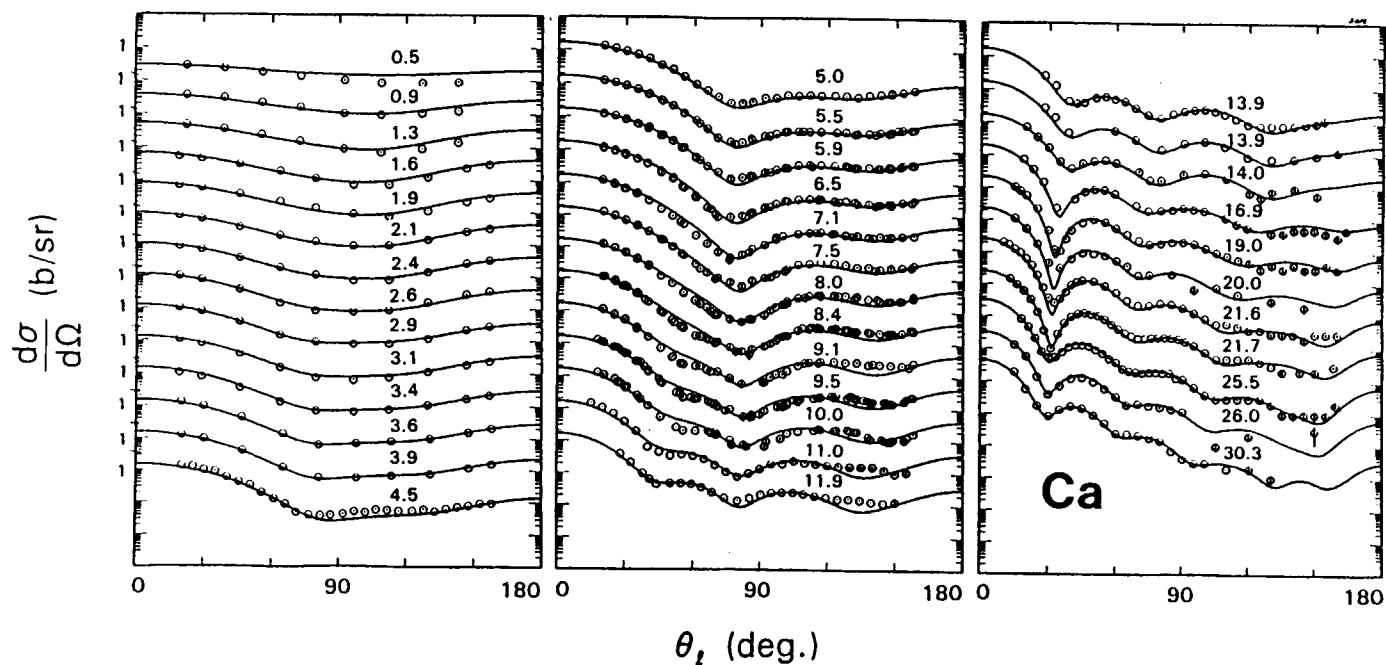
Fig. IV-1. Comparison of calculated (curves) and measured (symbols) differential elastic-scattering cross sections. The calculations used the SOM of Table IV-1. Incident-neutron energies are numerically noted in MeV.
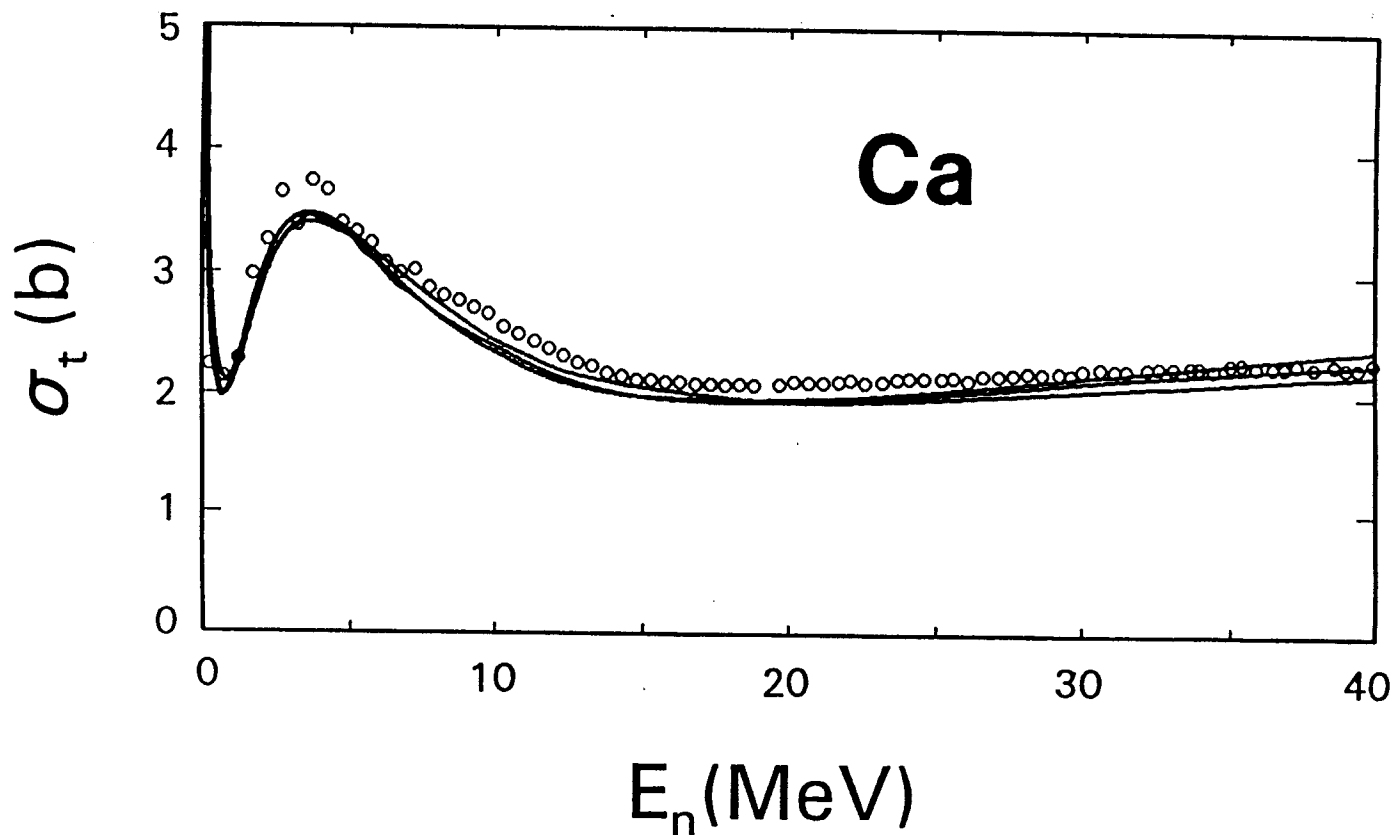
Fig. IV-2. Comparison of a 500 keV average of measured (symbols) [LHH80] and calculated (curves) neutron total cross sections of calcium. The calculations employed the SOM, DOM and CCM of the text. At ≈ 10 MeV the SOM curve is the lowest, followed by the CCM result and then the DOM values. At ≈ 40 MeV the DOM result is lowest, followed by CCM and then SOM results.

Ca

$$A_y(\theta)$$

θ_ℓ (deg.)
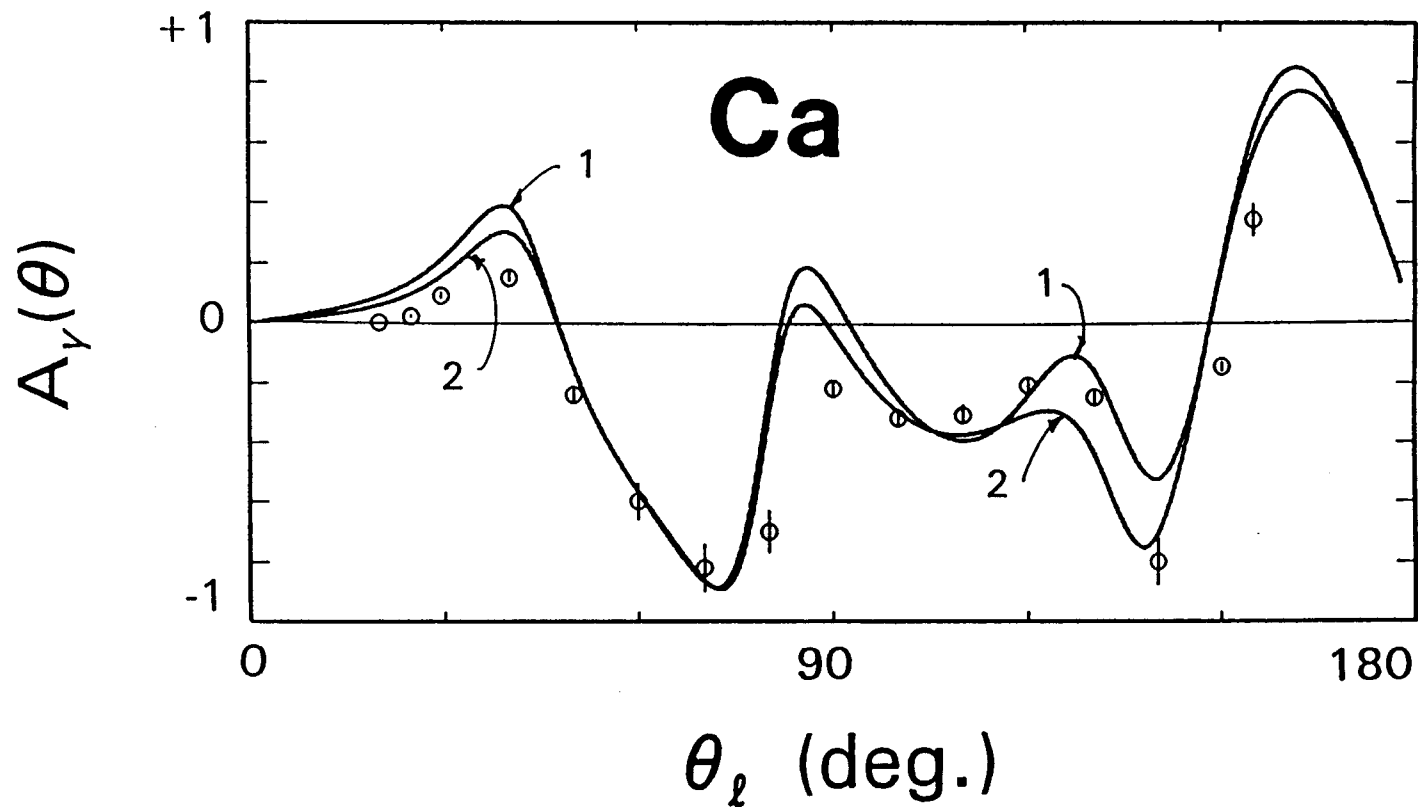
Fig. IV-3. Comparison of measured (symbols) [Tor+86. Hon+86] and calculated (curves) polarizations of 11.9 MeV elastically-scatter neutrons. Calculations employed the SOM ("1") and the CCM ("2") parameters, as described in the text.

$$V(r,E) = V_{HF}(r,E) + \frac{P}{\pi} \int_{-\infty}^{+\infty} \frac{V(r,E')dE'}{(E-E')}, \qquad \text{(IV-2)}$$

where P denotes the principal value of the integral and V_{HF} is the local-equivalent Hartree-Fock potential. This relationship results in the "Fermi Surface Anomaly" which leads to a departure of the real strength from V_{HF} at lower energies. The expression of Eq. IV-2 will impact on the parameters of the SOM deduced from the observed data. The consequences were examined by re-fitting the experimental data base using the DOM, including the contributions of the integral of Eq. IV-2.

It is convenient to evaluate Eq. IV-2 in terms of the volume integrals per nucleon, J_i. Formulated in that manner, Eq. IV-2 becomes

$$J_V = J_{HF} + \frac{P}{\pi} \int_{-\infty}^{+\infty} \frac{J_W(E')dE'}{(E-E')}, \qquad \text{(IV-3)}$$

where the integral can be broken into surface, ΔJ_S, and volume, ΔJ_{VO}, components. Then

$$\Delta J_S(E) = \frac{P}{\pi} \int_{-\infty}^{+\infty} \frac{J_S(E')dE'}{(E-E')}$$

$$\qquad \qquad \qquad \qquad \text{(IV-4)}$$

$$\Delta J_{VO}(E) = \frac{P}{\pi} \int_{-\infty}^{+\infty} \frac{J_{VO}(E')dE'}{(E-E')},$$

and

$$J_V(E) = J_{eff}(E) + \Delta J_S(E), \qquad \text{(IV-5)}$$

where $J_{eff}(E) = J_{HF}(E) + \Delta J_{VO}(E)$. In the present SOM interpretations, there is no experimental support for a volume absorption to at least an energy of ≈ 22 MeV. Furthermore, it has been shown that ΔJ_{VO} is an approximately linear function of the energy for $-25 \le E \le 25$ MeV [Chi+92], with a zero magnitude at the Fermi Energy, E_F. As J_{HF} is approximately a linear function of energy over the same energy range, one can not experimentally distinguish the J_{HF} and ΔJ_{VO} contributions to $J_{eff}(E)$. It is useful to define the ratio

$$\lambda(E) = \Delta J_S(E)/J_S(E), \qquad \text{(IV-6)}$$

where $\lambda(E)$ is the quantity by which the surface-imaginary potential, J_s, is multiplied by to give the surface-peaked component of the real potential, ΔJ_s.

$\lambda(E)$, Eq. IV-6, was initially evaluated using the SOM deduced above, and re-determined at each step of the iterative fitting procedure. The calculation was carried out using a simple, and frequently used approach. J_s was assumed to be symmetric about E_F, where E_F was taken to be - 12 MeV. For energies $2 \cdot E_F < E < 0$, J_s was assumed to have the parabolic form $J_s = (J_0/E_F^2)(E-E_F)^2$, where J_0 is the value of J_s at $E = 0$. For $0 < E < 22$ MeV, J_s was taken to have the linear form deduced from the fitting of the experimental data base. Above $E = 22$ MeV, J_s was assumed to linearly decrease with energy to a zero value at 60 MeV. This assumption is consistent with that of ref. [Hon+86]. Alternate choices of the 60 MeV end point had small effects on the calculation of the above integral. The assumptions suggest that volume absorption sets in at ≈ 22 MeV, and increases in a linear manner to ≈ 60 MeV. The ΔJ_s behavior calculated with these assumptions is shown in Fig. IV-4, and Fig. IV-5 shows the corresponding $\lambda(E)$ values. ΔJ_s is zero at E_F, and $\lambda(E)$ decreases from rather large values at $E = 0$ MeV, to zero at ≈ 17 MeV, and then becomes negative. The effect is to add a significant surface term to the SW Hartree-Fock real potential at low energies, and to subtract a surface term at high energies. The above calculational approach has been employed several times at this laboratory [Chi+92, Smi+92].

With the above approximations, and the $\lambda(E)$ of Eq. IV-6, the entire fitting procedure, outlined above in the context of the SOM, was repeated, including two iterative adjustments of both the (n,X) channel competition and the calculation of $\lambda(E)$. The resulting DOM potential parameters are given in Table IV-2. The SOM and DOM potential parameters are reasonably consistent. The real-potential diffusenesses are similar, with that of the DOM slightly smaller as one expects at lower energies since a small surface component of the potential has been removed through the dispersion integral of Eq. IV-2. The r_v and r_{veff} are similar at lower energies, but that of the DOM is somewhat larger at higher energies. Both real strengths, J_v and J_{eff}, decrease with energy, but the slope and zero-energy intercept of J_{eff} are considerably less. This is to be expected as the J_{eff} does not include the ΔJ_s of Eq. IV-5, which, from Fig. IV-4, is ≈ 40 MeV-fm^3 at zero energy and deceases with energy. The fact that the differences between J_{eff} and J_v are not entirely accounted for by ΔJ_s reflects the contribution from ΔJ_{vo} (illustrated in
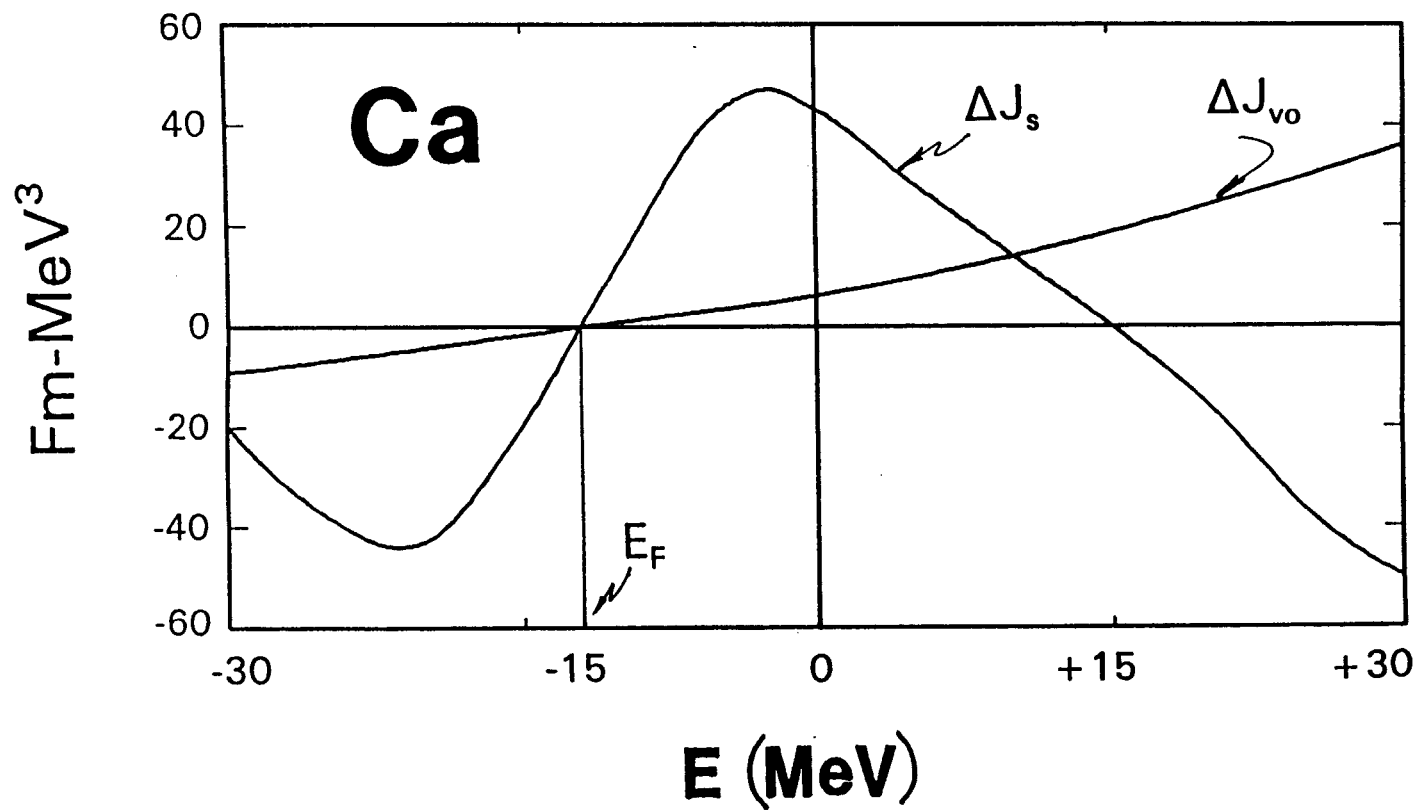
Fig. IV-4. Energy dependence of ΔJ_s and of ΔJ_{vo} of Eq. IV-4, calculated as described in the text.
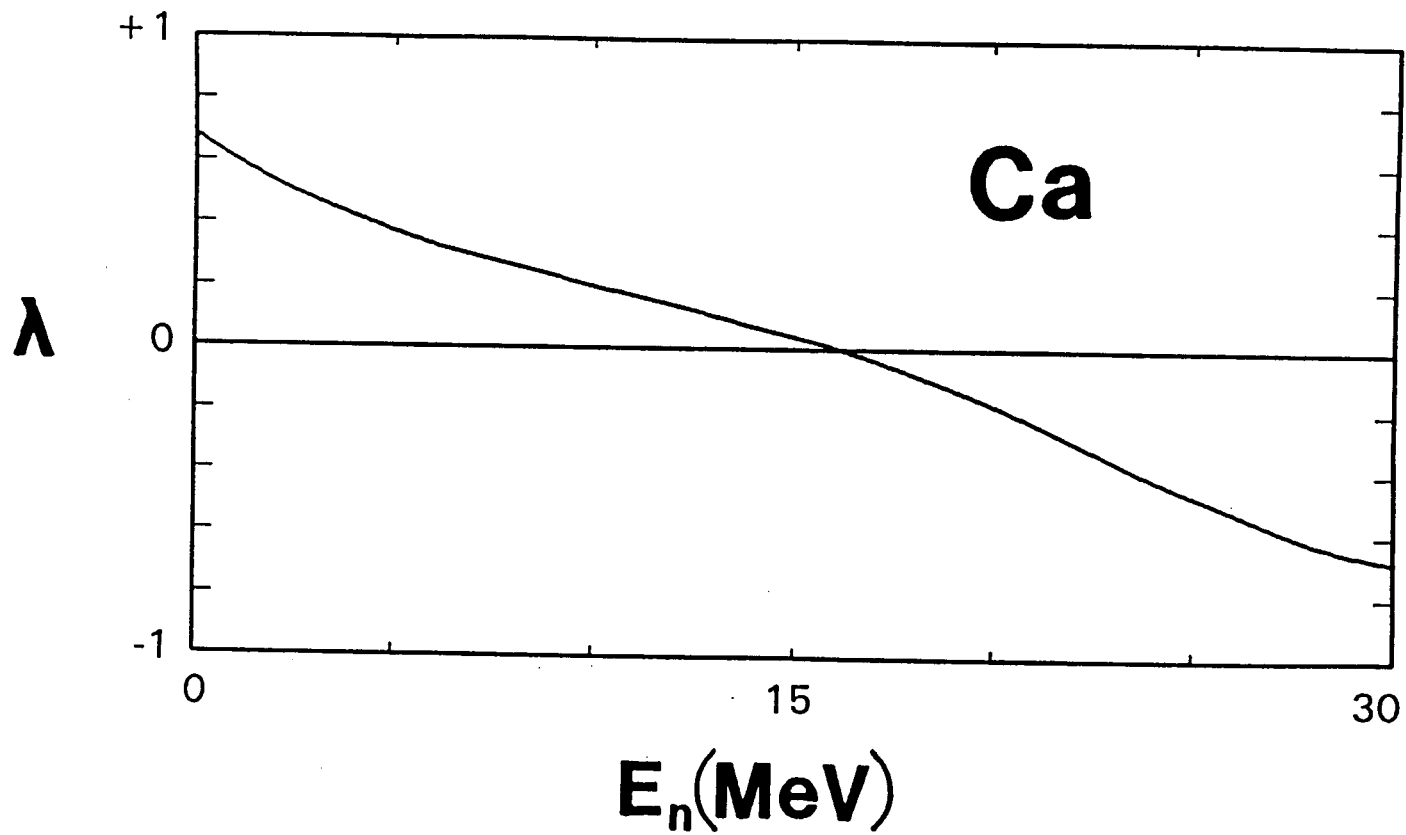
Fig. IV-5. Energy dependence of $\lambda(E)$ of Eq. IV-6.

Fig. IV-4) included in J_{eff}. The imaginary-parameters of the SOM and DOM are less well determined, but even so the differences are qualitatively reasonable. The r_w are essentially identical below ≈ 11 MeV. At very high energies, r_w of the SOM tends to be larger. This probably reflects the energy dependence of $\lambda(E)$ (Fig. IV-5). The SOM and DOM a_w's are qualitatively similar, and both have quite small values at zero energy. The SOM and DOM J_w's have the same qualitative character, rising with energy as more channels open and then approaching similar plateau values at higher energies. Generally, the impact of the dispersion relationship is most felt on the real potential.

Comparison of calculated SOM and DOM results with the neutron data offers little guidance. The calculated differential elastic-scattering distributions are very similar to one another and to the experimental values (see Figs. IV-1 and -6). There is similar agreement between calculated and measured total cross sections, as illustrated in Fig. IV-2. As in the SOM case, the DOM model derivation implies (n,X) cross sections that are 10 → 15% smaller than given in ENDF/B-VI.

IV-5 Coupled-Channels Model (CCM)

It was assumed that the 3⁻ state at 3.7367 MeV is a collective surface-vibrational level, and the subsequent 2⁺ (3.9044 MeV) and 5⁻ (4.4914 MeV) levels are very likely of the same character [Tam65]. The observed inelastic-scattering cross sections for the combined excitation of the first two of these levels are very much larger than predicted by CN contributions at higher energies (see Fig. III-5), though the anisotropy of the corresponding differential distributions is not particularly strong until one is above 10 MeV [Hon+86, AR87]. It has been argued that the collective interactions significantly effect the calculations of neutron polarizations [DT88, Hon+86].

In view of the above considerations, the present interpretations were extended to include collective surface-vibrational coupling. The calculational vehicle was the coupled-channels code ANLECIS [Mol81]. The β of the (3⁻)level was assumed equal to 0.329, that for the (2⁺) level equal to 0.088, and for the (5⁻) level equal to 0.243. These β values are consistent with those given in refs. [Hon+86, Bai+77 and [AR87], and their implications are discussed in Section V. Comprehensive coupled-channels fitting, as applied in the SOM and DOM contexts, is very time consuming, therefore some simplifying assumptions were made. The procedure generally followed that of the

Table IV-2. DOM potential parameters. The nomenclature is identical to that of Table IV-1.

Real Potential

$$J_{eff} = 480.0 - 0.3125 \cdot E$$
$$r_{veff} = 1.160 + 0.0147 \cdot E \quad (E < 10)$$
$$r_{veff} = 1.3069 \quad (E \geq 10)$$
$$a_{veff} = 0.5628$$

Imaginary Potential

$$J_{w} = 46.0 + 4.50 \cdot E \quad (E < 12 \text{ MeV})$$
$$J_{w} = 100.0 \quad (E \geq 12)$$
$$r_{w} = 1.360 - 0.0079 \cdot E$$
$$a_{w} = 0.20 + 0.0377 \cdot E \quad (E < 10)$$
$$a_{w} = 0.5760 \quad (E \geq 10)$$
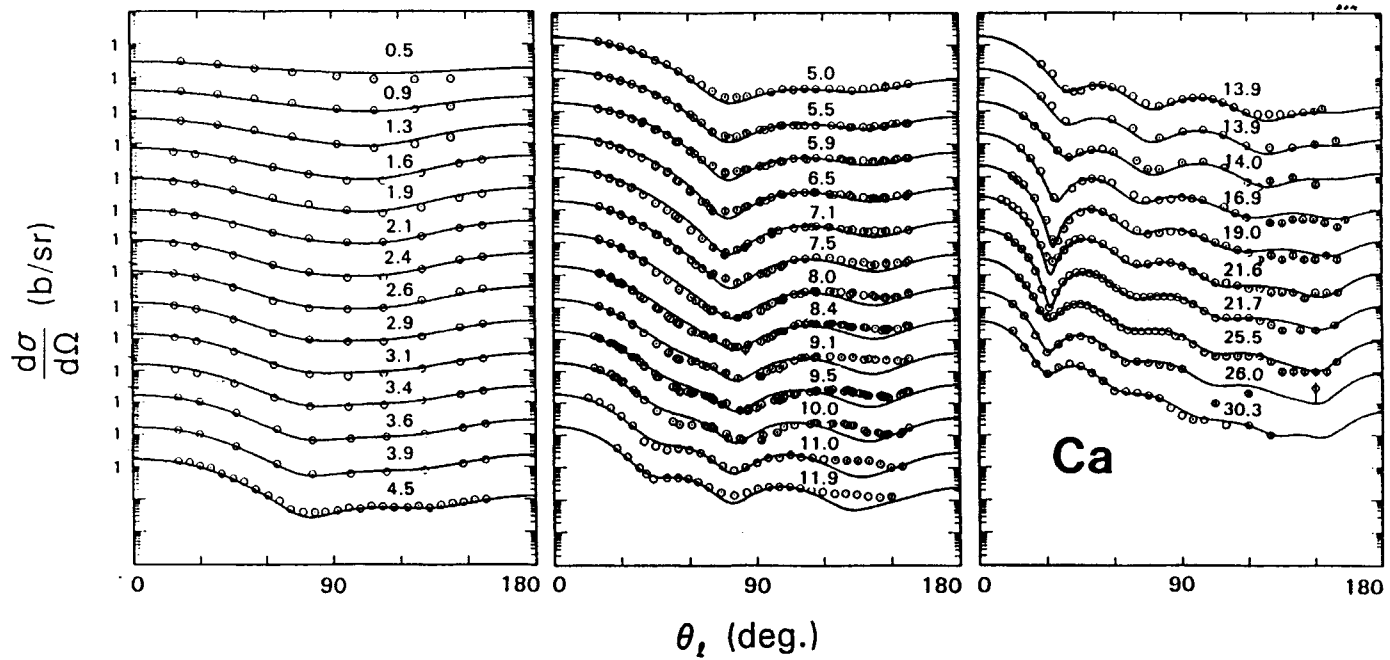
Spin-Orbit Potential (Same as given in Table IV-1)

Fig. IV-6. Comparison of measured (symbols) and calculated (curves) differential elastic-scattering cross sections of calcium. The calculations employed the DOM of Table IV-2. The notation is identical to that of Fig. IV-1.

SE fitting outlined above, with adjustment of the CE contribution to obtain SE cross sections for fitting and three iterations to determine the competition with the (n,X) processes. The fitting considered the coupling of the ground, 3^-, 2^+ and 5^-, though the observed excitations of the latter level are relatively small. This is the same coupling scheme as employed in refs. [Hon+88 and AR87]. The geometries of the SOM were assumed, and the fitting confined to the real- and imaginary-potential strengths.

The the real- and imaginary-potential strengths resulting from the coupled-channel fitting are given in Table IV-3. The real CCM potential strength is similar to that of the SOM, with differences that are probably not significant. The CCM and SOM imaginary strengths are also similar, although the CCM representation increases linearly with energy over the entire energy range of the interpretations (i,e., from E = 0 → 30 MeV), but with less slope. The CCM gives essentially the same description of the observed elastic scattering as the SOM (which is illustrated in Fig. IV-1). Similarly, the CCM total cross sections and polarizations agree rather well with those obtained with the SOM, as illustrated in Figs. IV-2 and -3. In the case of the polarizations, the CCM approach is arguably superior. It is only in the higher-energy inelastic-scattering cross sections that the CCM leads to pronounced improvement, as shown in Fig. III-5. CN inelastic · scattering does not account for the observed higher-energy inelastic scattering while the composite of CCM and CN contributions is in quite good agreement with the observations over all energies. The simple coupling of the present CCM also describes the inelastic-scattering angular distributions at higher energies, as illustrated by the comparisons of Fig. IV-7. Generally, the CCM model leads to results as descriptive of the higher-energy observables as those obtained with models specifically tailored to those energies and inelastic-scattering reactions [Hon+85, ARF87, AR87].

V. DISCUSSION

The real-potential diffusenesses of the present SOM (and CCM) and DOM are energy independent and generally smaller than the systematic trends reported in the literature and noted at this laboratory [SG92, RB67, JM88, DT88, Hon+86, Tor+82 and ARF87]. The differences are not large, ≈ 0.05 fm. Intuitively, it is not surprising that the ^{40}Ca real-potential diffuseness may be somewhat smaller than that predicted by global trends as the doubly-magic target can be expected to have a "hard" surface.

The real-potential radii of the present SOM (and CCM) and DOM, at higher energies where the parameters are energy independent, are ≈ 6 → 8% larger than generally resulting from phenomenological studies

Table IV-3. Strengths of real and imaginary CCM potential expressed in terms of volume-integrals-per-nucleon. The relevant notation is identical to that of Table IV-1.

Real Potential

$$J_V = 496.0 - 2.27 \cdot E$$

Imaginary potential

$$J_W = 52.0 + 1.80 \cdot E$$
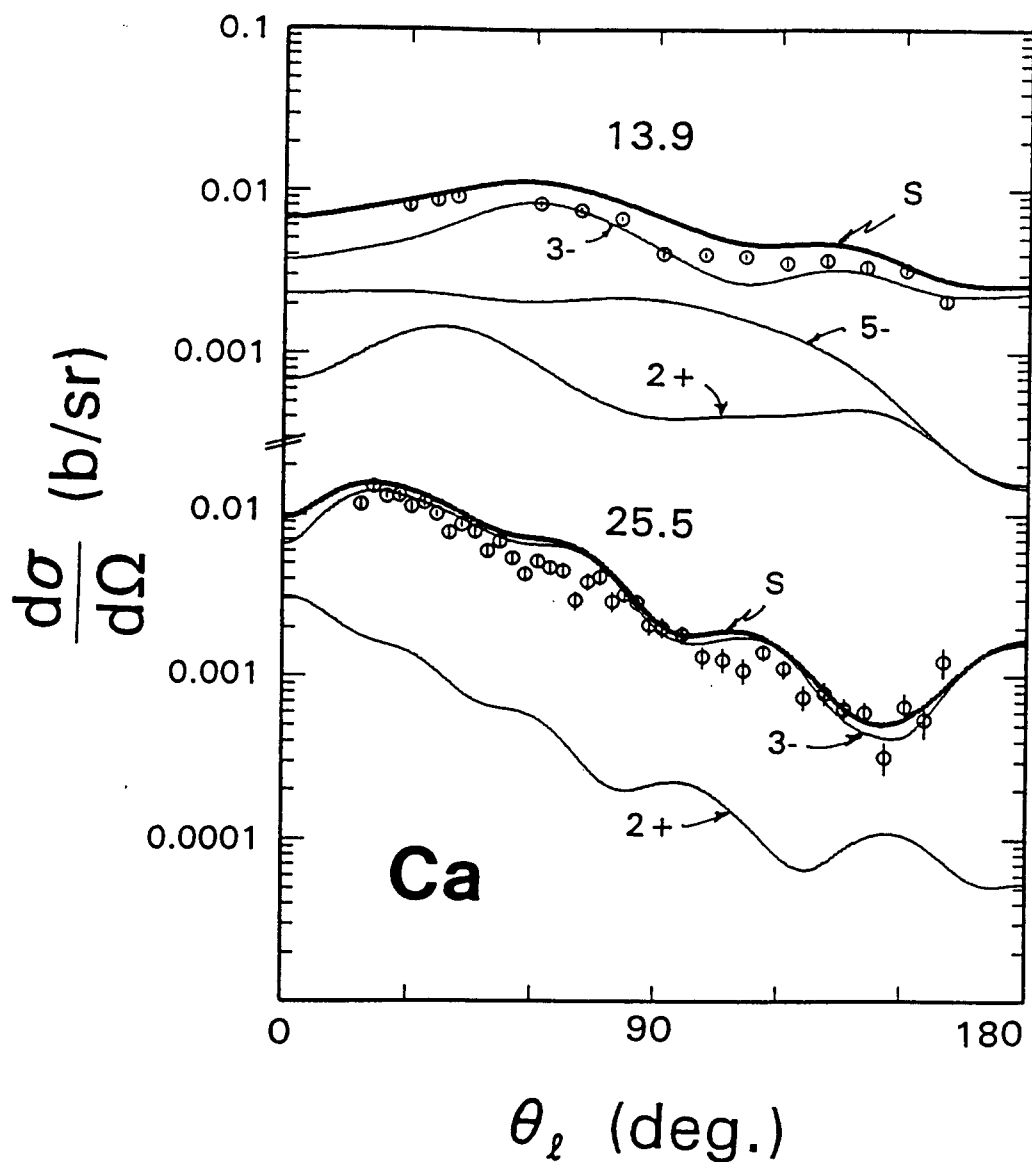
Fig. IV-7. Comparison of measured (symbols) and CCM calculated (curves) cross sections for the excitation of 3.74 + 3.95 and 4 levels of ^{40}Ca. The upper portion of the figure is at 13.9 MeV, using the data of ref. [Hon+86]. The lower portion is at 25.5 MeV, using the data of ref. [AR87]. Light curves indicate the calculated excitations contributing to the observations, and the heavy curves the sum ("S") comparable with the measured values. Contributing J^π values are noted.

reported in the literature [RB67, JM88, DT88, Hon+86, Tor+82 and ARF87]. Even considering a strong correlation between the real-potential strength and radius, these are significant differences. However, the systematic behavior of SOM real-potential radii has been examined in refs. [SG92 and Chi+90]. Those studies were made at a neutron energy of 8 MeV where the contribution of the dispersion integral of Eq. IV-2 is small for most targets (this is less so for the present ^{40}Ca case due to the large negative value of E_F). From these considerations it was found that the mass dependence of the SW r_v of the SOM is given by

$$r_v = r_0 + r_1/A^{1/3}, \qquad (V-1)$$

where A is the mass number, $r_0 = 1.154$ fm, and $r_1 = 0.407$ fm. Eq. V-1 implies a r_v for ^{40}Ca of 1.273 fm, which is in remarkable agreement with the 8 MeV SOM and DOM results of the present phenomenological interpretations. In addition, it has recently been shown that Eq. V-1 is valid for neutron scattering from the similar light target ^{45}Sc [SG93]. Thus, the empirical expression of Eq. V-1 appears to be a reasonable "global" representation for the neutron SOM over a wide mass range extending form A $\approx$ 40 $\to$ 209. It is less valid when dealing with strong collective targets [SG93A].

Meyers [Mey73] has considered the geometric properties of leptodermous distributions. The SW distribution is one such, sometimes called the "fermi function". Meyers parameterizes such distributions in terms of the "equivalent sharp radius", R_s. R_s is somewhat larger than the R used in SW parameterizations, but the two are easily related using the SOM geometric parameters of Table IV-1. When this is done, the Meyers expression becomes

$$r_v = 1.096 + 0.425/A^{1/3}, \qquad (V-2)$$

where A is the target mass and r_v is the usual reduced real-potential radius. Meyers obtained the numerical constants of Eq. V-2 from a global survey of proton SOMs (the radii of proton SOMs have been reported smaller than those of neutron SOMs [ARF87]). The constants of Eqs. V-1 and V-2 are somewhat different but the mass dependence is the same. The important point is that both Eqs. V-1 and -2 indicate that the r_v of the SOM with a SW form factor increases with decreasing target mass. This is consistent with the present ^{40}Ca SOM and the systematics of phenomenological SOM studies [SG92, Chi+90]. However, the conclusion is in contrast to that of some other phenomenological investigations [Var+87]. It has been suggested [SG93, Chi+90] that the neutron SOM real-potential strength, at 8 MeV, follows a

systematic behavior given by

$$J_v = K_0 \cdot [\; 1 - \xi((N-Z)/A)] \cdot (r_0 + r_1/A^{1/3})^3, \qquad (V\text{-}3)$$

where $K_0 = 236\!:\!1$ MeV, $\xi = 0.575$, and r_0 and r_1 follow from Eq. V-1.

Eq. V-3 obviously reduces to $J_v = K_0 \cdot (r_0 + r_1/A^{1/3})^3 = 487.07$ MeV-fm^3

for ^{40}Ca, which is within 0.98% of the 482.32 MeV-fm^3 value implied by Table IV-1. This result gives further support to the systematic behavior described by Eqs. V-1 and -3, and to the present ^{40}Ca SOM parameterization.

The r_v of the SOM and the r_{veff} of the DOM are not the same thing and can not be directly compared. However, Tables IV-1 and IV-2 and the $\lambda(E)$ of Fig. IV-5 can be used to calculate the equivalent root-mean-square (RMS) radii of the two models. The results are in very good agreement with the largest differences at the lower energies where, for example, at 1 MeV the discrepancy is $\approx 1.3\%$. The real-potential radii of all the present interpretations decrease as the energy decreases to small values. Mahaux and Sartor [MS86] have examined the energy dependence of the RMS real radius in the context of the dispersion relationship. They considered n + ^{208}Pb, p + ^{208}Pb and p + ^{40}Ca systems. The results for the p + ^{40}Ca system were erratic or inconclusive, in a large part due to the lack of reliable low-energy data. For the ^{208}Pb cases, the real-potential RMS radius was predicted to decrease rather sharply with decreasing energy at low energies. This prediction is consistent with the trends of Tables IV-1 and -2. Perhaps the detailed low-energy results of the present work support the predictions of ref. [MS86].

The present SOM J_v is qualitatively similar to many values quoted in the literature [RB67, JM88, DT88, Hon+86, Tor+82, ARF87, and BG69]. The E $\rightarrow$ 0 literature values of J_v range from ≈ 460 to 525 MeV-fm^3,

with the majority of them clumped about 500 MeV-fm^3. The energy dependencies are not always well defined due to the limited energy scope of the data, but the slopes are approximately linear and qualitatively similar. Comparisons at selected higher energies, such as given in Table V-1, are a measure of these slopes. The present results are very consistent with those of refs. [Tor+82 and Hon+86], and are somewhat larger than the results of refs. [ARF87 and AR87]. The majority of the results indicate little difference between SOM and CCM J_v values, but one should be cautious of that conclusion as SOM and CCM geometries are the same at each institution. The J_{eff} of the DOM, Table IV-2, is smaller than J_v, as it must be since the J_{eff} of

Eq. IV-5 is not the Hartree-Fock component, since it includes the ΔJ_{vo} component of Eq. IV-4 (and Fig. IV-5). ΔJ_{vo} leads to a slope of J_{eff} that is considerably less than that of J_{HF}. The present J_v values are consistent with those of the neighboring ^{45}Sc [SG93]. Eq. V-3 leads to a ^{45}Sc J_v at 8 MeV $\approx$ 4.5% smaller than that of ^{40}Ca. The comparable experimentally-deduced J_v values differ by $\approx$ 1.5%. The experimental potentials were derived quite independently, thus the small discrepancy between phenomenological and systematic results is probably not significant.

Optical potentials have been developed from microscopic nucleon-nucleon theory. They tend to take two forms. In one case the mass operator in infinite nuclear matter is calculated and then a local density approximation is used to adapt the result to finite nuclei [JLM76]. On the other hand, an explicit representation of the effective interaction is obtained and the optical potential deduced by folding this interaction with nuclear-matter density. The latter method was used by Brieva and Rook [BR78] to predict the $^{40}Ca(n,n)$ processes at the energies of the present work. Their results lead to a value of J_v as $E \to 0$ that is in essentially exact agreement with the phenomenological value of Table IV-1. Unfortunately, the predicted dJ_v/dE value is approximately a factor of two larger than the present phenomenological value, or most of those found in the literature.

A number of broad-ranging SOM real potentials have been proposed, frequently for equation-of-state considerations. These are generally based upon proton potentials as only they are available in an energy scope of perhaps - 100 $\to$ +100 MeV. In such expressions, the energy region within $\approx |25|$ MeV of E_F is generally avoided as not being representative of the wide energy-dependent trends. This type of general SOM real-potential is illustrated by the work of Bauer et al. [Bau+82]. Those authors suggest a general real potential of the form

$$V = 52.4 - 0.37 \cdot E + 0.0007 \cdot E^2, \qquad (V-4)$$

where the additional coulomb and isovector terms have been dropped as they are not applicable to the present case of neutron scattering from ^{40}Ca. Eq. V-4 can be expressed in the volume-integral form,

$$J_v = 511.2 - 3.609 \cdot E + 0.0068 \cdot E^2, \qquad (V-5)$$

using the geometries of ref. [Bau+82]. Eq. V-5 is in reasonable agreement with the present SOM J_v (Table IV-1). At E = 0 the difference is 1.5%, at 10 MeV 0.2%, and at 20 MeV 1.8%. The agreement

with the J_{eff} of the DOM is less satisfactory. This is not surprising as Eq. V-5 essentially represents the local-equivalent Hartree-Fock potential while $J_{eff} = J_{HF} + \Delta J_{vo}$. Eq. V-5 should be compared with $J_{eff} - \Delta J_{vo}$, where ΔJ_{vo} is shown in Fig.-4. When that is done the comparisons with Eq. V-5 are much improved. Unfortunately, ΔJ_{vo} can not be directly determined from experiment, and even the contribution of volume absorption to the model is not well defined.

The theory of dynamic vibrations of Brown el al. [Bro+79] treats the region near the Fermi Surface. The reduced mass, m^*, is given by

$$\frac{m^*}{m} = 0.64 + 0.36 \cdot [\ 1\ +\ |E-E_F|/2\hbar\omega_0\ ]^{-2}, \qquad (V-6)$$

and $dV/dE = 1 - m^*/m$. Assuming $\hbar\omega_0 = 41/A^{1/3}$ [Bro+79], Eq. V-6 leads to $dJ_v/dE \approx -2.11$, using the present SOM geometries. This result is consistent with the SOM of Table IV-1, however the magnitude is much larger than the dJ_{eff}/dE of Table IV-2. Again, the difference is in the ΔJ_{vo}. Assuming $\frac{m^*}{m} = 1 - dV/dE$ and the energy-dependent geometries of Table IV-1, one finds that the ratio m^*/m decreases as one goes from ≈ 8 MeV to zero energy.

Throughout the present interpretations it has been assumed that the real potential has the conventional SW form. That assumption constrains the considerations, and may lead to a systematic bias of the results. Several authors (e.g., [ARF87] and [Tor+82]) have considered this possibility in the context of neutron scattering from ^{40}Ca using "model independent approximations" (MIA). In the latter approach, the SW potential is supplemented by a low-order fourier-bessel expansion [FB78], extending over $\approx 5 \rightarrow 10$ terms. Predictably, the descriptions of the experimental data are superior to those obtained with the SW potential alone as a number of additional parameters are involved. The information content of the experimental data used in such interpretations is limited by scope and by statistical and systematic uncertainties. This information is spread over many more parameters in the MIA approach, with the consequence of rather large parameter uncertainties. The effect of the latter is particularly acute at small radii. In view of these uncertainties, it is not surprising that the results of MIA investigations are "mixed". For example, the work of ref. [Tor+82] suggests a deviation from the SW form, particularly at small radii where the MIA strength is greater than that of the SW form. Such a trend is supported by some nuclear-structure calculations [BNV74]. On the other hand, the MIA interpretations of ref. [ARF87] give results that are reasonably close

to the SW form at energies relevant to the present work. Achieving more definitive MIA results will require a new degree of experimental precision at higher energies where inherent physical effects, such as CN fluctuations, are not further complicating factors. Such data is beyond the energy range of the present measurements, the interpretation of which is already complicated not only by fluctuations, but also by collective effects and strong and uncertain CN channel competition. Thus, it is not realistic to examine the present experimental results in the context of the MIA. It is suggested that, when a MIA interpretation is attempted, some alternative to the fourier-bessel expansion be considered in order to reduce the number of parameters involved and limit the radial oscillations of the results, perhaps a simple gaussian or poisson increment to the conventional SW potential.

The imaginary potential is not as well defined as the real potential in the present work, and in the literature; influenced as it is by nuclear-structure effects, particularly the fluctuations of the CN processes at lower energies. However, the imaginary-potential radius at low energies (e.g., $E \to 0$) is much larger than the real potential in all of the present interpretations. Extensive other work at this laboratory, in particular studies of neutron scattering from ^{45}Sc, has displayed the same effect (e.g., ref. [Chi+90 and SG93] and refs. cited therein). This low-energy effect is valid regardless of which model is used. Furthermore, it is consistent with the generally large imaginary radii reported in low-energy (e.g., strength function) studies in the literature [Mol63, MDH81]. These large imaginary radii decrease with energy and in the range $10 \to 20$ MeV approach an energy independent value that, in the present work, is approximately the same as that of the real-potential radii. The deviation of the present DOM imaginary radius at higher energies from the latter trend is probably a fitting anomaly. Previous studies reported in the literature are generally at energies of more than 10 MeV so they can shed little light on the low-energy behavior. Moreover, the previously-reported imaginary-potential radii scatter by considerable amounts [RB67, JM88, DT88, Hon+86, Tor+82 and ARF87].

The imaginary potential diffusenesses of the present work rise from small magnitudes at $E = 0$ to values only slightly less than those of the real potential at $10 \to 15$ MeV. The latter are relatively consistent with a number of the results reported in the literature from higher-energy studies [RB67, JM88, DT88, Hon+86, Tor+82 and ARF87]. This type of behavior has been observed in many studies at this laboratory (e.g. ref. [Chi+90]), and specifically in the scattering from the nearby ^{45}Sc nucleus [SG93]). Intuitively, one would expect the absorption to be increasingly confined to the nuclear surface as the energy decreases, at very low energies approaching a delta function. The present work, and that reported in the literature, assumes a surface absorption of the SW-derivative form, and possibly at higher energies ($E \approx> 22$ MeV) a volume absorption of the SW form with the same parameters as the real potential. Repeated

attempts to identify a volume absorption in the present work were not successful. This is not surprising as the majority of the data base is below ≈ 22 MeV, and refs. [Hon+86 and ARF87] suggest that volume absorption becomes significant only above ≈ 22 MeV. There is only one high-quality distribution above ≈ 22 MeV (at 25.5 MeV [ARF87]), and the remainder of the high-energy data base does not have the detail necessary for unequivocally determining the presence of volume absorption. Good quality total cross sections do extend to much higher energies but they alone do not provide rigorous model definition. In detail, the common practice of assuming a volume absorption at higher energies is very likely wrong. More probable is an absorption that is confined to a narrow edge of the nuclear surface at low energies, that spreads to the nuclear interior with increasing energy, and finally approaches a uniform volume absorption. Some microscopic potentials tend to support such a behavior [JLM76]. The conventional use of energy-dependent surface and volume absorptions is a very crude mockup of the probable reality. The matter seems to have never been phenomenologically investigated in detail. To do so would require some very excellent elastic-scattering data. The tendency of the present phenomenological models to have smaller imaginary- than real-potential radii at higher energies (e.g., at ≈ 25 MeV) may reflect a movement of the absorption toward the interior of the nucleus.

The imaginary-potential strengths of the present work are ≈ 50 MeV-fm^3 at E = 0, increase with energy to 12 → 20 MeV and then approach a constant value of 100 → 110 MeV-fm^3 at higher energies. In the present work a linear-segment representation was used. Refs. [JM88 and BR81] suggest the form

$$J(E)_W = B \cdot \frac{(E-E_F)^2}{(E-E_F)^2 + \epsilon^2} , \qquad (V-7)$$

which is probably more realistic than the linear segments used here. The parameters of Eq. V-7 are not well defined by the experimental data, but with B = 130 MeV-fm^3 and ϵ = 16 MeV Eq. V-7 is similar to the linear-segment representation of Table IV-1. The present imaginary strengths are reasonably consistent with those reported in the literature for neutron scattering from ^{40}Ca at higher energies [ARF87, AR87], and for similar processes dealing with magic nuclei [Chi+90]. The strength for scattering from the neighboring ^{45}Sc is larger at low energies [SG93] as ^{45}Sc is not magic and the number of levels not explicitly treated in the model is much larger than is the case of ^{40}Ca.

The spin-orbit potential of the present work was taken from the real spin-orbit potential of ref. [Hon+86], which was developed from detailed polarization studies. Thus it is not surprising that the present potentials do reasonably well in describing the observed elastic-scattering polarizations, as illustrated in Fig. IV-3. Ref. [Hon+86] includes a small imaginary spin-orbit potential. Ref. [DT88] considered the impact of the dispersion relationship on the calculation of polarizations, and it was concluded that an imaginary spin-orbit potential is not necessary. Both considerations may lead to improvements, but if so they are of modest proportions. The simple real spin-orbit potential used here gives an experimental description that is very nearly as good, if not as good, as that achieved with the additional complexities. All of the polarization calculations are significantly discrepant with the observed values in some prominent facets of the reaction.

In the context of phenomenological neutron scattering and total cross sections, there is very little to choose between the SOM and the DOM. Both give essentially the same description of the physical observables and both have energy dependent parameters differing in an understandable way. Clearly, the dispersion integral alone falls far short of entirely explaining these energy dependencies. Other physical effects must be active. The effect of the dispersion integral is felt primarily at bound energies (see below). It should be remembered that either the SOM or the DOM of the present work describe the total and elastic-scattering cross sections over the entire energy range 0 → 30+ MeV to acceptable accuracy. It is partly a matter of energy-dependent changes in the surface absorption, but the imaginary diffuseness does decrease and the imaginary radius increases with decreasing energy as qualitatively suggested in ref. [JM88]. These changes, along with those of the real potential, are now quantitatively defined. With them there appears to be no justification for calling upon added complexities such as l-dependent potentials. Inelastic scattering indicates that the CN process will not account for the measured results as the cross section magnitudes are significant at higher energies where many channels are open, and the angular distributions of the inelastically-scattered neutrons are highly anisotropic [Tor+82, AR87].

The present CCM accounts for the elastic- and inelastic-scattering, neutron polarizations, and total cross sections (as illustrated in Figs. III-5, IV-2, IV-3 and IV-7) using a relatively simple coupling scheme. In view of this success, no attempt was made to adjust the β_λ deformation parameters. The accepted β_λ values, and other relevant model parameters, are supported by additional considerations. The deformation lengths at higher energies, δ_λ ($\delta_\lambda \equiv \beta_\lambda \cdot R$), following from the present CCM are δ_3 = 1.437 and δ_5 = 1.061 fm. These values are to be compared with ≈ 1.33 and 0.93 of ref. [AR87] and 1.41 ± 0.08 and 1.02 ± 0.15 of ref.

[Bai+77], respectively. One must be a bit careful of comparing δ_λ values as they will be energy dependent if the geometric parameter, R, is energy dependent. The present comparisons are made at energies where R is reasonably constant. Using the method of Hamilton and Mackintosh [HM78], and as applied in ref. [AR87], one can calculate the moment of the real vibrational field q_λ, and then the normalized moment $Q_\lambda = q_\lambda/J_v$, and also the $B(E3) = (Z \cdot Q_{30})^2 \cdot e^2$, for the G.S. → 3⁻ transition in ^{40}Ca. In the 21 → 26 MeV region the present work gives $Q_{30} = 7.34$ fm^3 and $B(E3)^{1/2} = 146.8$ e·fm^3. The latter value is somewhat larger than the corresponding EM result of 133 - 139 [Eis+69, EL78, Law80] but closer than the 162 - 176 result of ref. [AR87], depending on integration range. This improvement tends to support the larger real-potential radius of the present work, in addition to the assumed β_3 values.

The above DOM can be extrapolated beyond the experimental energy range, particularly to the bound-state regime, and it is there that the effect of the dispersion integral of Eqs. IV-2 or -3 is most evident. The dispersion relationship holds for the radial moments of the potential, where

$$\langle r(E)^q \rangle_V = \langle r(E)^q \rangle_{HF} + \frac{P}{\pi} \int_{-\infty}^{+\infty} \frac{\langle r(E')^q \rangle_W}{(E-E')} \, dE', \qquad (V-8)$$

and

$$\langle r(E)^q \rangle_W = \frac{4\pi}{A} \int_0^\infty W(r,E) \, r^q \, dr. \qquad (V-9)$$

Mahaux and Sartor have examined the radial moments for stability, and have selected q = 0.8, 2 and 4 as best defined by experimental information [MS85]. Their choice is followed here. Using these three moments, the potential is extrapolated to E < 0 (i.e., to the shell-model potential). This approach has been extensively used by Mahaux and co-workers, and at this laboratory [LGS89, Chi+90]. The moments were determined from the potential of Table IV-1, which is based upon neutron elastic scattering data at energies of less than ≈ 30 MeV. The energy dependence of the imaginary-potential moments was taken to be that of Brown and Rho [BR81],

$$\langle r(E)^q \rangle_W = \frac{C_q (E-E_F)^2}{(E-E_F)^2 + D_q^2}. \qquad (V-10)$$

The energy dependence of the moments of the Hartree-Fock real

potential were assumed to have the linear form

$$\langle r(E)^q \rangle_{HF} = A_q + B_q \cdot E, \qquad (V\text{-}11)$$

which is generally consistent with Eq. V-5 over the limited energy range of the present considerations. Combining Eqs. V-8, -10 and -11, one can express the real-potential moments in the form

$$\langle r(E)^q \rangle_v = A_q + B_q \cdot E + \frac{C_q D_q (E - E_F)}{(E - E_F)^2 + D_q^2} . \qquad (V\text{-}12)$$

Using the imaginary-potential strengths and geometries from Table IV-1 the moments were calculated at a number of energies distributed over the range $E = 0 \rightarrow 30$ MeV and the constants C_q and D_q determined by fitting, with the results given in Table V-2. D_q is nearly constant as the energy-dependent shapes of the three moments are similar while C_q is clearly the infinite-energy limit of Eq. V-10. Having determined C_q and D_q, the real-potential moments can be calculated from the parameters of Table IV-1 and Eq. V-12 and used to determine the constants A_q and B_q by fitting. The resulting values are given in Table V-3.

Eq. V-12 was assumed to hold in the bound-state region, and the corresponding SW potential parameters were calculated from the constants of Tables V-2 and -3. The spin-orbit potential parameters were taken from Table IV-1. The resulting SW potential, based on neutron-scattering data, implies the binding energies of particle- and hole-states as given in column three of Table V-4. The binding energies are remarkably well predicted considering that: i) large energy extrapolations are required (particularly for the deep hole states), ii) considerable numerical manipulations are involved, and iii) the results are quite sensitive to the HF constants A_q and B_q. The latter sensitivity was examined by repeating the entire set of calculations only limiting the scattering data upon which they were based to $E \geq 8$ MeV (i.e., to energies where the geometry of the real potential is constant). The resulting calculated binding energies had the same qualitative trends as shown in Table V-4 but the magnitudes were consistently lower than the experimentally-deduced values by one to several MeV.

Since ^{40}Ca is a $T = 0$ target, several authors have examined the correlation of p + ^{40}Ca and n+ ^{40}Ca potentials and the coulomb energy shift [Hon+86, ARF87]. The emphasis of the present work is on lower and bound energies where the proton reactions are greatly inhibited, or even forbidden, by the coulomb barrier. Thus no attempt was made

41

Table V-1. Comparison of SOM and CCM J_v values (in MeV-fm^3) at E_n = 21.7 and 25.5 MeV.

Reference	21.7 MeV	25.5 MeV
SOM, present work	445.5	434.9
CCM, present work	446.7	438.1
SOM, [Tor+82]	442.8	432.4
CCM, [Hon+86]	448.0	438.3
SOM, [ARF87]	435.0	417.0
CCM, [AR87]	420.7	405.2

Table V-2. The parameters C_q and D_q of Eq. V-9.

Parameter	Moment (q)		
	0.8	2.0	4.0
C_q	21.0	135.0	3100.0
D_q	15.0	17.0	17.0

Table V-3. The parameters A_q and B_q of Eq. V-11.

Parameter	Moment (q)		
	0.8	2.0	4.0
A_q	120.63	432.86	6154.0
B_q	-0.783	-1.939	-5.419

Table V-4. Measured and calculated binding energies of particle and hole states.

State	Binding Energy (MeV)	
	Exp.[a]	Scattering Data
$0d_{5/2}$	≈ 22.5	23.87
$1s_{1/2}$	18.1	17.94
$0d_{3/2}$	15.6	16.63
$0f_{7/2}$	8.4	8.61
$1p_{3/2}$	6.0	5.30
$1p_{1/2}$	4.0	3.70
RMS dev.[b]		0.70

[a] Taken from [EL78].

[b] RMS deviation from experimental values.

to repeat the comparisons of neutron and proton potentials of previous work as there is probably little that can be added without new extensive, precise and higher-energy measurements and their interpretations. Such measurements were not a part of the present work.

The above remarks assume that the observables are consistent with the concepts of the optical model, and generally free of local structure effects. However, this is not clearly so. Careful inspection of the energy-averaged total cross section (see Fig. IV-2) reveals a broad "hump" centered about 10 - 12 MeV. It is of small magnitude, but inconsistent with the present, or similar, model concepts. The present model descriptions (and those of a number of other authors) of the observed elastic-scattering distributions are not particularly good in the same ≈ 10 - 12 MeV region. Unfortunately, the large majority of the available polarization information is in this questionable energy region. The problem has not been generally recognized, although there have been attempts to improve the description of the experimental observables using l-dependent potentials [KM79], MIA interpretations [Ala+85], and coupling to giant resonances [Hon+86]. The success has been "mixed". At the energies of the present measurements one should not expect to have explicit agreement between results obtained with simple models and the experimental values. More complex models, and precise data to justify them, will be necessary to resolve these issues.

At lower energies the present calculations are sensitive to CN processes and the associated channel competition. Therefore, the large values of the (n,p) and (n,α) cross sections are a concern. The present interpretations, based upon neutron scattering, suggest that the composite of the commonly accepted (n,α) and (n,p) cross sections [ENDF] is too large by 10 - 15%. This may be a significant concern in some applications.

ACKNOWLEDGEMENT

<u>REFERENCES</u>

Abr+71   D. Abramson et al., NEA Report, EANDC(E)-149 (1971); data available from the National Nuclear Data Center, Brookhaven National Laboratory.

Ala+85   R. Alarcon, J. Rapaport, D. Wang and Y. Wang, Bull. Am. Phys. Soc. <u>30</u> 796 (1985).

AR87   R. Alarcon and J. Rapaport, Nucl. Phys. <u>A462</u> 445 (1987).

ARF87   R. Alarcon, J. Rapaport and R. Finlay, Nucl. Phys. <u>A462</u> 413 (1987).

Bai+77   D. E. Bainum, R. W. Finlay, J. Rapaport, J. D. Carlson and W. G. Love, Phys. Rev. <u>C16</u> 1377 (1977).

Bau+82   M. Bauer, H. Hernandez-Saldana, P. E. Hodgson and J. Quintanilla, J. Phys. <u>G8</u> 525 (1982).

BG69   F. G. Becchetti and G. W. Greenlees, Phys. Rev. <u>182</u> 1190 (1969).

BNV74   A. Boussey, N. Ngo and N. Vihn Mau, Proc. Conf. on Nuclear Structure and Spectroscopy (Scholar's Press, Amsterdam, 1974).

BQ81   C. M. Bartle and P. A. Quin, Ann. Nucl. Energy <u>8</u> 43 (1981).

BR78   F. A. Brieva and J. R. Rook, Nucl. Phys. <u>A307</u> 493 (1978).

BR81   G. E. Brown and M. Rho, Nucl. Phys. <u>A372</u> 397 (1981).

Bro+79   G. E. Brown, J. S. DeHea and J. Speth, Nucl. Phys. <u>A330</u> 290 (1979).

Bud+84   C. Budtz-Jorgensen, P. Guenther, A. Smith, J. Whalen, W. McMurray, M. Renan and I. van Heerden, Z. Phys. <u>A319</u> 47 (1984).

CL55   L. Cranberg and J. Levin, Proc. Inter. Conf. on Peaceful Uses of Atomic Energy (IAEA Press, Vienna, 1955).

CSL82   <u>Nuclear Standards File</u>, IAEA Technical Report 227, Editors H. Conde, A. Smith and A. Lorenz (IAEA Press, Vienna, 1982).

Chi+90   S. Chiba, P. Guenther, R. Lawson and A. Smith, Phys. Rev. <u>C42</u> 2487 (1990).

Chi+92   S. Chiba, P. Guenther, A. Smith, M. Sugimoto and R. D. Lawson, Phys. Rev. <u>C45</u> 1260 (1992).

Dev+81   R. P. Devito, S. M. Austin, W. Sterrenberg and V. E. Borg, Phys. Rev. Lett. <u>47</u> 628 (1981).

Dro87   M. Drosg, Production of monoenergetic neutrons between 0.1 and 23 MeV; Neutron energies and cross sections, IAEA-TECDOC-410, 239 (IAEA Press, Vienna, 1987).

DT88   J. P. Delaroche and W. Tornow, Phys. Lett. B<u>203</u> 4 (1988).

Eis+69   R. A. Eisenstein et al., Phys. Rev. <u>188</u> 1815 (1969)

ENDF   Calcium evaluated nuclear data file-B, version VI, Evaluators F. Perey and C. Fu, available from the National Nuclear Data Center, Brookhaven National Laboratory.

EL78   P. M. Endt and C. Van de Leun, Nucl. Phys. <u>A310</u> 561 (1978).

FB78   E. Friedman and C. J. Batty, Phys. Rev. <u>C17</u> 34 (1978).

FCR77   J. C. Ferrer, J. D. Carlson and J. Rapaport, Nucl. Phys. <u>A275</u> 325 (1977).

Fra+64   A. J. Frasca, R. V. Finlay, R. D. Kosheland and R. L. Cassola, Phys. Rev. <u>144</u> 854 (1964).

GC65   A. Gilbert and A. Cameron, Can. J. Phys. <u>43</u> 1446 (1965).

Gue77   P. T. Guenther, PhD Thesis, University of Illinois (1977).

HF52   V. Hauser and H. Feshbach, Phys. Rev. <u>87</u> 362 (1952).

Hic+90   S. F. Hicks, S. E. Hicks, G. R. Shen and M. T. McEllistrem, Phys. Rev. <u>C41</u> 2560 (1990).

HM78   J. K. Hamilton and R. S. Mackintosh, J. Phys. <u>G4</u> 557 (1978).

Hod71   P. E. Hodgson, <u>Nuclear Reactions and Nuclear Structure</u> (Clarendon, Oxford, 1971).

Hof+75   H. M. Hofmann, J. Richert, J. V. Tepel and H. A. Weidenmuller, Ann. Phys. (NY) <u>90</u> 406 (1975).

Hol+69   B. Holmqvist, T. Viedling, S. G. Johansson, G. Lodin, A. Kiss, B. Gustavsson and B. Anta, Aktiebolaget Atomenergi Report, AE-366 (1969).

Hon+86   G. M. Honore, V. Tornow, C. R. Howell, R. S. Pedroni, R. C. Byrd, R. L. Valter and J. P. Delaroche, Phys. Rev. <u>C33</u> 1129 (1986).

JLM76   J. P. Jeukenne, A. Lejeune and C. Mahaux, Phys. Reports <u>C25</u> 83 (1976).

JM88   C. H. Johnson and C. Mahaux, Phys. Rev. <u>C38</u> 2589 (1988).

KM79   A. M. Kobos and R. S. Mackintosh, J. Phys. <u>G5</u> 97 (1979).

Lan+66   R. O. Lane, A. S. Langsdorf Jr., J. E. Monahan and A. Elwyn, Ann. Phys. <u>12</u> 135 (1966).

Law80   R. D. Lawson, <u>Theory of the Nuclear Shell Model</u> (Clarendon, Oxford, 1980).

LGS89   R. D. Lawson, P. T. Guenther and A. B. Smith, Nucl. Phys. <u>A493</u> 267 (1989).

LHH80   D. C. Larson, D. M. Hetrick and J. A. Harvey, Bull. Am. Phys. Soc. <u>25</u> 543 (1980).

MDH81   S. F. Mughabghab, M. Divadeenam and N. E. Holden, <u>Neutron Cross Sections</u> (Academic, New York, 1981).

Mey73   V. D. Meyers, Nucl. Phys. <u>A204</u> 465 (1973).

MN82   C. Mahaux and H. Ngo, Nucl. Phys. <u>A378</u> 205 (1982).

Mol63   P. A. Moldauer, Nucl. Phys. <u>47</u> 63 (1963).

Mol80   P. A. Moldauer, Nucl. Phys. <u>A344</u> 185 (1980).

Mol81   P. A. Moldauer, The coupled-channels computer code ANLECIS, private communication (1981); a modification of ECIS-79 by J. Raynal, NEA technical memorandum (1979).

Mol82   P. A. Moldauer, The spherical optical-statistical code ABAREX, private communication (1982).

MS85   C. Mahaux and R. Sartor, NEA Report, NEANDC-222U (1985).

MS86   C. Mahaux and R. Sartor, Nucl. Phys. <u>A460</u> 466 (1986).

MS86A   C. Mahaux and R. Sartor, Nucl. Phys. <u>A451</u> 441 (1986).

MS88   C. Mahaux and R. Sartor, Nucl. Phys. <u>A484</u> 205 (1988).

NNDC   National Nuclear Data Center, Brookhaven National Laboratory.

Ols+87   N. Olsson, B. Trostell, E. Ramstroem and B. Holmqvist, Nucl. Phys. <u>A472</u> 237 (1987).

OTR+90   N. Olsson, B. Trostell and E. Ramstroem, Nucl. Phys. <u>A513</u> 205 (1990).

PK70   F. G. Perey and V. E. Kinney, Oak Ridge National Laboratory Report, ORNL-4519 (1970).

Rap+77   J. Rapaport, J. D. Carlson, D. Bainum, T. S. Cheema and R. Finlay, Nucl. Phys. $\underline{A286}$ 232(1977).

RB67   J. D. Reber and J. D. Brandenberger, Phys. Rev. $\underline{163}$ 1077 (1967).

Sat83   G. R. Satchler, <u>Direct Nuclear Reactions</u> (Clarendon, Oxford, 1983).

SG82   A. B. Smith and P. T. Guenther, Argonne National Laboratory Report, ANL/NDM-65 (1982).

SG92   A. B. Smith and P. T. Guenther, Argonne National Laboratory Report, ANL/NDM-125 (1992).

SG93   A. B. Smith and P. T. Guenther, J. Phys. $\underline{G19}$ 655 (1993)

SG93A   A. B. Smith and P. T. Guenther, to be published in Nucl. Phys.

SGM82   A. B. Smith, P. T. Guenther and R. D. McKnight, Proc. Conf. on Nucl. Data for Science and Technology, p.-39, Editor K. H. Boeckhoff (Reidel, Dordrecht, Holland, 1982).

SGS77   A. B. Smith, P. T. Guenther and R. Sjoblum, Nucl. Instruments and Methods $\underline{140}$ 397 (1977).

Smi+67   A. Smith, P. Guenther, R. Larson, C. Nelson, P. Walker and J. Whalen, Nucl. Instruments and Methods, $\underline{50}$ 277 (1967).

Smi88   A. B. Smith, Monte-Carlo correction codes, unpublished Argonne National Laboratory memorandum (1988).

Smi+92   A. B. Smith, P. T. Guenther, J. F. Whalen and S. Chiba, J. Phys. $\underline{G19}$ 629 (1992).

Smi93   A. B. Smith, to be published.

Tam65   T. Tamura, Rev. Mod. Phys. $\underline{37}$ 679 (1965).

Tor+82   W. Tornow, E. Woye, G. Mack, C. E. Floyd, P. P. Guss, S. A. Wender, R. C. Byrd, R. L. Walter, T. B. Clegg and H. Leeb, Nucl. Phys. $\underline{A385}$ 373 (1982).

Var+87   R. L. Varner, T. B. Clegg, T. L. McAbee and W. J. Thompson, Phys. Lett. $\underline{B185}$ 6 (1987).